

To appear in the *Astronomical Journal*, August 2002

## Molecular Gas in Elliptical Galaxies: Distribution and Kinematics

L. M. Young

*Physics Department, New Mexico Institute of Mining and Technology, Socorro, NM 87801*

lyoung@physics.nmt.edu

### ABSTRACT

I present interferometric images ( $\sim 7''$  resolution) of CO emission in five elliptical galaxies and nondetections in two others. These data double the number of elliptical galaxies whose CO emission has been fully mapped. The sample galaxies have  $10^8$  to  $5 \times 10^9 M_\odot$  of molecular gas distributed in mostly symmetric rotating disks with diameters of 2 to 12 kpc. Four out of the five molecular disks show remarkable alignment with the optical major axes of their host galaxies. The molecular masses are a few percent of the total dynamical masses which are implied if the gas is on circular orbits. If the molecular gas forms stars, it will make rotationally supported stellar disks which will be very similar in character to the stellar disks now known to be present in many ellipticals. Comparison of stellar kinematics to gas kinematics in NGC 4476 implies that the molecular gas did not come from internal stellar mass loss because the specific angular momentum of the gas is about three times larger than that of the stars.

*Subject headings:* galaxies: individual (UGC 1503, NGC 807, NGC 3656, NGC 4476, NGC 5666, NGC 4649, NGC 7468) — galaxies: elliptical and lenticular, cD — galaxies: ISM — galaxies: kinematics and dynamics — galaxies: evolution — ISM: molecules

### 1. Introduction

It is now well known that elliptical galaxies often do have interstellar media with some cold neutral gas and dust. Huchtmeier, Sage, & Henkel (1995) have found that about two thirds of ellipticals in the RSA catalog contain HI at levels  $M(HI)/L_B \geq 10^{-3}$  in solar units; Wardle & Knapp (1986) reach similar conclusions. Colbert, Mulchaey, & Zabludoff (2001) find that dust is apparent in optical images of about 75% of all ellipticals regardless of their environment (field vs. X-ray detected poor groups). The molecular gas content of ellipticals is more difficult to quantify because, with few exceptions, only the ones which are bright in the far-IR (FIR) have been searched. However, Knapp & Rupen (1996) quote CO detection rates of 20 to 80% for ellipticals which are brighter than 1 Jy at  $100\mu\text{m}$ .

Since it was believed for many years that elliptical galaxies have little or no cold molecular gas, detailed studies of that molecular gas can offer fundamental insight into the evolution of ellipticals. For example, one would obviously like to know the origin of the molecular gas. Did it come from internal sources (stellar mass loss) or from an external source (another galaxy)? Has it been there for a Hubble time or significantly less? The distribution and kinematics of the molecular gas, and particularly comparisons of the specific angular momentum of the gas and the stars, can help clarify the origin of the molecular gas. Molecular gas is also the raw material for star formation. Therefore, the properties of the molecular gas determine where and how much star formation can happen; this determines the future morphology of the galaxy. Finally, molecular gas distribution and kinematics are valuable because the dissipational nature of gas means that the shapes of the gas orbits are much better known than are the stellar orbits (e.g. de Zeeuw & Franx (1989); Cretton, Rix, & de Zeeuw (2000)). Gas kinematics can be used to infer the galaxy potential in a way which is more robust than, or at least complementary to, what one can do with stellar kinematics. This paper uses high resolution CO observations to investigate these ideas about elliptical galaxy structure and evolution.

Several authors have used single-dish telescopes to search for CO emission from ellipticals. The largest of these works are Lees et al. (1991), Wiklind, Combes, & Henkel (1995), and Knapp & Rupen (1996). A very small number of elliptical galaxies have been mapped in CO with millimeter interferometers or with multiple pointings on single dish telescopes. These include NGC 759 (Wiklind, Combes, Henkel, & Wyrowski 1997), NGC 1275 (Reuter, Pohl, Lesch, & Sievers 1993; Braine et al. 1995; Inoue et al. 1996), NGC 7252 (Wang, Schweizer, & Scoville 1992), NGC 1316 (Horellou et al. 2001), and NGC 5128 = Cen A (Quillen, de Zeeuw, Phinney, & Phillips 1992; Rydbeck et al. 1993; Charmandaris, Combes, & van der Hulst 2000). In all of these galaxies except NGC 7252, molecular gas is found in a rotating disk on the order of a kpc or a few kpc in radius and containing about  $10^9 M_{\odot}$  of  $H_2$ . In Cen A, a nearby galaxy which permits detailed observations, the large scale CO disk closely follows the prominent optical dust lane and is strongly warped (Quillen, de Zeeuw, Phinney, & Phillips 1992). About 10% of the CO in Cen A is associated with stellar and HI shells at galactocentric radii of 15 kpc (Charmandaris, Combes, & van der Hulst 2000). The CO in NGC 7252, a merger remnant, has compact but irregular structure and kinematics.

The present paper doubles the number of elliptical galaxies with CO maps; I show images of CO emission in five elliptical galaxies and nondetections in two others. In addition, the present sample is valuable because it employs a clearly-defined set of selection criteria (in contrast to the semi-random collection of interesting galaxies mentioned above).

## 2. Sample selection

The observed galaxies were chosen from a survey of CO emission in ellipticals that was made with the IRAM 30m telescope by Wiklind, Combes, & Henkel (1995) [WCH]. WCH, Lees et al. (1991), Gordon (1991), Sage & Wrobel (1989), Knapp & Rupen (1996), and several other sets of

authors selected galaxies for single dish CO surveys based on a combination of IRAS 60  $\mu\text{m}$  and 100  $\mu\text{m}$  fluxes and galaxy type. The most common FIR flux criterion (used by WCH and all of the surveys mentioned here except Sage & Wrobel (1989)) is  $S_{100\mu\text{m}} > 1.0$  Jy, where the 100  $\mu\text{m}$  fluxes were taken from the compilation of Knapp, Guhathakurta, Kim, & Jura (1989). WCH attempted to pick out “genuine” ellipticals by restricting their sample to galaxies known to have an  $r^{1/4}$  profile or, in their words, “a consistent classification as E in several catalogs.” Those criteria defined a sample of 29 ellipticals, of which 16 were detected in CO.

The present sample contains all but one of the galaxies that were detected by WCH with  $^{12}\text{CO}$  1-0 integrated intensities greater than  $5.0 \text{ K km s}^{-1}$  ( $23 \text{ Jy km s}^{-1}$ ) and that lie within the declination range accessible to BIMA and OVRO. NGC 759, which also meets these criteria, was excluded because a high resolution CO map of this galaxy has already been published (Wiklind, Combes, Henkel, & Wyrowski 1997). To this list I also added NGC 4649, for which a CO detection is reported by Sage & Wrobel (1989). The resulting sample is given in Table 1.

There is significant overlap between the sample selected here from the survey of WCH and other single dish CO surveys. NGC 5666 and NGC 4476 have the second and third highest CO 2-1 intensities in the sample of 24 galaxies studied by Lees et al. (1991). NGC 5666 has the highest CO 2-1 intensity in the sample of seven ellipticals studied by Gordon (1991).

The galaxies observed by WCH are found almost evenly divided among the field, groups, and clusters. Of the galaxies observed here, three are classified by WCH as being field ellipticals, one is a member of a small group, two are in the Virgo cluster, and one is most likely a merger remnant. If molecular gas is associated with dust, then this distribution of environments is consistent with the study of Colbert, Mulchaey, & Zabludoff (2001), who found that optical signatures of dust are found in field ellipticals at the same rate as in ellipticals in X-ray bright groups. Additional discussion of selection effects in the present sample can be found in section 5.5.

### 3. Observations and data reduction

#### 3.1. BIMA data

Six galaxies [UGC 1503, NGC 807, NGC 3656, NGC 4476, NGC 4649, and NGC 5666] were observed with the 10-element Berkeley-Illinois-Maryland Association (BIMA) millimeter interferometer at Hat Creek, CA (Welch et al. 1996). The BIMA observations were carried out in the C configuration (projected baselines 3 to 34  $\text{k}\lambda$ ) between November 1998 and June 2001. One additional track in the D configuration was obtained for NGC 5666 in March 1999, giving projected baselines down to 2.3  $\text{k}\lambda$  for that galaxy.

Each galaxy was observed with a single pointing centered on the optical center of the galaxy; the primary beam FWHM is about  $100''$ . Each observation covered a velocity range of about  $1000 \text{ km s}^{-1}$  centered on the velocity of the CO detected by WCH. The optical velocities of the galaxies

Table 1. Sample Galaxies

Galaxy	RA J2000.0	Dec	Velocity km/s	Distance Mpc	$L_B$ $10^{10} L_\odot$	Environment
UGC 1503	02 01 19.8	+33 19 46	5086 (6)	69	1.7	field
NGC 807	02 04 55.7	+28 59 15	4764 (12)	64	3.2	field
NGC 3656	11 23 38.4	+53 50 31	2869 (13)	45	1.6	merger remnant
NGC 4476	12 29 59.2	+12 20 55	1978 (12)	18	0.35	Virgo cluster
NGC 4649	12 43 39.6	+11 33 09	1117 (6)	18	6.7	Virgo cluster
NGC 5666	14 13 09.1	+10 30 37	2221 (6)	35	0.63	field
NGC 7468	23 02 59.3	+16 36 19	2081 (6)	28	0.39	group

Note. — Velocities are taken from the NASA Extragalactic Database (NED); they refer to HI where available or to stellar velocities. The distance estimates are taken from WCH, who used  $H_0 = 75 \text{ km s}^{-1} \text{ Mpc}^{-1}$  and a Virgocentric infall model which is described in their paper. The members of the Virgo cluster were assumed to be at 18 Mpc. Blue luminosities are taken from integrated magnitudes in RC3; environmental descriptors are taken from WCH.

are uncertain by up to  $100 \text{ km s}^{-1}$  but are always well within the velocity range covered. Table 1 gives some basic data for the sample galaxies and Table 2 summarizes important parameters of the observations and the final images.

Reduction of the BIMA data was carried out using standard tasks in the MIRIAD package (Sault, Teuben, & Wright 1995). Electrical line length calibration was applied to most of the tracks, with a few exceptions in cases where the measurement was too noisy to be useful or where the line length was a very smooth function of time. Data from an atmospheric phase monitor (Lay 1999) were used to estimate the magnitude of amplitude decorrelation, as described by Regan et al. (2001) and Wong (2001). A small interferometer with a fixed 100 meter baseline measures the rms path length difference in the signal from a commercial broadcast satellite; those data are scaled to the observing frequency and are scaled by projected baseline length raised to the 5/6 power to estimate the amount of amplitude decorrelation in the data (Akeson 1998). An rms path length difference of  $300 \mu\text{m}$  on a 100 m baseline produces an amplitude decorrelation of 0.82 for observations at 3mm wavelength (Akeson 1998), but the longest baseline in the present data is 88 m. Twelve tracks with rms path lengths less than  $300 \mu\text{m}$  were not explicitly corrected for decorrelation because normal amplitude calibration can take out most of the decorrelation effect (Wong 2001). Fourteen tracks with rms path lengths in the range  $300\text{--}700 \mu\text{m}$  were corrected using the MIRIAD task *uvdecor*, which multiplies up the data amplitudes to correct for decorrelation losses and decreases the weights of data with large decorrelation losses. Data with larger rms path lengths than  $700\mu\text{m}$  were generally not used. The worst track that was used had a median amplitude correction factor of 1.15. Amplitude corrections were applied to all observed sources and calibrators before the absolute flux calibration was made.

Absolute flux calibration was based on observations of Uranus or Mars. When suitable planets were not available, the secondary calibrator 3C273, which is usually monitored several times per month, was used (see Table 2). Phase drifts as a function of time were corrected by means of a nearby calibrator observed every 30 to 40 minutes. Gain variations as a function of frequency were corrected by the online passband calibration system; inspection of the data for 3C273 indicate that residual passband variations are on the order of 10% or less in amplitude and  $2^\circ$  in phase across the entire band.

The calibrated visibility data were weighted by the inverse square of the system temperature and the inverse square of the amplitude decorrelation correction factor, then Fourier transformed. No continuum emission was evident in the line-free channels of any galaxy (Table 3). The dirty images were lightly deconvolved with the Clark clean algorithm, as appropriate for these compact, rather low signal-to-noise detections. Integrated intensity and velocity field maps were produced by the masking method: the deconvolved image cube was smoothed along both spatial and velocity axes, and the smoothed cube was clipped at about  $2.5\sigma$  in absolute value. The clipped version of the cube was used as a mask to define a three-dimensional volume in which the emission is integrated over velocity. This masking method is described in greater detail by Wong (2001) and by Regan et al. (2001).

Table 2. Observation and Image Parameters

Galaxy	Observation dates	Fluxcal	Velocity Range km s <sup>-1</sup>	Beam "	Linear res. kpc	Channel km s <sup>-1</sup>	noise mJy b <sup>-1</sup>
UGC 1503	2000 Nov – 2001 June	uranus	4530–5580	7.10×6.26	2.4×2.1	30	8.5
NGC 807	2000 Dec – 2001 May	uranus	4230–5280	7.00×6.34	2.2×2.0	30	8.0
				9.43×8.46	2.9×2.6	50	6.8
NGC 3656	2000 Mar, Apr	3c273	2375–3335	7.76×6.16	1.7×1.3	30	16
						20	19
NGC 4476	2000 Mar, Apr	3c273/saturn	1480–2440	8.29×5.66	0.73×0.49	30	11
						20	13
NGC 4649	2000 May	3c273	450–1800	8.22×6.07	0.72×0.53	30	24
NGC 5666	1998 Nov – 1999 Apr	mars/3c279	1865–2555	10.32×7.63	1.7×1.3	30	15
				8.27×5.99	1.4×1.0	30	17
NGC 7468	2001 Apr, May	uranus/3c454.3	1628–2772	6.54×5.45	0.89×0.74	20.8	13

Table 3. Continuum Flux Density  
Limits

Galaxy	3mm continuum mJy
UGC 1503	<5.0
NGC 807	<5.4
NGC 3656	<13
NGC 4476	<7.0
NGC 4649	<12
NGC 5666	<13
NGC 7468	<5.3

Note. — Continuum images were made by averaging all of the line-free channels in the final image cubes. The values quoted here are 3 times the rms noise in the continuum images, so they should be interpreted as flux density limits for point sources at the centers of their host galaxies.

### 3.2. OVRO data

One galaxy, NGC 7468, was observed with the 6-element Owens Valley Radio Observatory (OVRO) millimeter interferometer (Padin et al. 1991). Those data were obtained in the C, L, and E configurations (projected baselines 4 to 44 k $\lambda$ ) during April and May 2001. A single pointing was made on the optical center of the galaxy; the primary beam FWHM was about 65". The correlator was set up with four modules of 32 channels, each channel 4 MHz wide; the modules were overlapped to cover a total bandwidth of 464 MHz. The data were calibrated using the MMA package (Scoville et al. 1993). Absolute flux calibration was based on observations of Uranus; the passband and time-dependent phase calibration used the nearby source 3C454.3. The calibrated data were mapped in AIPS using “natural” weighting. Subsequent image analysis was identical to that for the BIMA data.

## 4. Results

### 4.1. Nondetections

No CO emission was detected in the data cubes for NGC 4649 or NGC 7468. Upper limits to the CO fluxes from these galaxies were determined by first summing the data cube over a square region 22.5" on a side, centered on the optical center of the galaxy, to produce a spectrum. The 22.5" region was chosen to be similar in size and area to the beam of the IRAM 30m telescope. A spectrum was also produced for a 55" square region (similar to the area of the NRAO 12m telescope) for NGC 4649. Nothing but noise is apparent in the spectra (Figures 1 and 2). The spectra were then summed over the velocity ranges described below. The uncertainty in the sum is calculated from the rms in the spectrum and the number of channels summed, as described by Young (2000) and Lees et al. (1991);  $3\sigma$  limits are given in Table 4. This estimate assumes the channels are uncorrelated, which is an excellent assumption for these data since no baseline or continuum emission needs to be subtracted.

WCH reported a detection, which they characterize as tentative, of  $6.7 \text{ K km s}^{-1} \sim 31 \text{ Jy km s}^{-1}$  in the  $^{12}\text{CO}$  1-0 line from NGC 7468. Their line is centered at  $2300 \text{ km s}^{-1}$  (220  $\text{km s}^{-1}$  distant from the optical velocity) and  $665 \text{ km s}^{-1}$  wide. The present OVRO observations give a sum of  $4.7 \pm 2.9 \text{ Jy km s}^{-1}$  over the 22.5" square region and over the same velocity range as the CO line of WCH. The OVRO data also give a sum of  $3.6 \pm 2.0 \text{ Jy km s}^{-1}$  over the same spatial region but over a  $300 \text{ km s}^{-1}$  velocity range centered on the HI velocity. (The HI line in NGC 7468 is about  $200 \text{ km s}^{-1}$  wide at 20% of peak intensity; see van Driel, Arnaboldi, Combes, & Sparke (2000).) Emission as strong as that reported by WCH should have been easily detected. I also consider it unlikely that CO in NGC 7468 is invisible to the interferometer by virtue of being smoothly distributed; the 23" beam of the 30m telescope is only three times larger than the 7" beam of the OVRO data, so the relevant spatial scales are well sampled in the interferometer data.



Table 4. H<sub>2</sub> Mass and Morphology

Galaxy	CO flux Jy km s <sup>-1</sup>	M(H <sub>2</sub> ) 10 <sup>8</sup> M <sub>⊙</sub>	CO diameter		CO shape		Kin Maj Ax
			"	kpc	ϵ	PA (°)	PA (°)
UGC 1503	32 (6)	18	30	11 (1)	0.37 (0.05)	−111 (1)	−123 (2)
NGC 807	29 (6)	14	40	12 (1)	0.58 (0.09)	143 (1)	149 (3)
NGC 3656	200 (20)	47	34	7.4 (0.7)	0.73 (0.02)	174.8 (0.1)	191 (3)
NGC 4476	30 (3)	1.1	27	2.4 (0.2)	0.57 (0.04)	−151 (1)	−152 (1)
NGC 4649	<18	<0.68	...	...	...	...	...
NGC 5666	39 (4)	5.7	28	4.7 (0.5)	0.11 (0.06)	166 (5)	165 (2)
NGC 7468	<6.2	<0.57	...	...	...	...	...

Note. — Upper limits are  $3\sigma$  for a  $22.5''$  square region and  $300 \text{ km s}^{-1}$  velocity range. See text for further information. Ellipticities and position angles (both morphological and kinematic) for the CO distributions are the median values from fits to three or four images made at different resolutions or with different clip levels. The values in parentheses for these last three columns are estimates of the uncertainty based on the spread among the different fits, because those spreads are always larger than the formal uncertainties of the fits. Position angles are measured North through East to the receding major axis.

Thus, the OVRO data for NGC 7468 confirm the nondetection of the 2-1 line of CO by Lees et al. (1991). Those authors quote an upper limit H<sub>2</sub> mass of  $8 \times 10^7 M_{\odot}$  (after scaling to the conversion factor and distance assumed here), which is consistent with the present  $6 \times 10^7 M_{\odot}$  limit. Details of the H<sub>2</sub> mass estimates are described in Section 4.2.

Sage & Wrobel (1989) report the detection of  $18.7 \pm 2.3 \text{ Jy km s}^{-1}$  of emission in <sup>12</sup>CO 1-0 from NGC 4649. Those observations were made with the NRAO 12m telescope, which has a beam of  $55''$ ; the reported line is  $225 \text{ km s}^{-1}$  wide. The detection is not considered tentative but again there is a rather large offset ( $200 \text{ km s}^{-1}$ ) between the CO velocity and the optical velocity. A sum over a  $55''$  box and over the same velocity range noted by Sage & Wrobel (1989) gives an integrated flux of  $33 \pm 18 \text{ Jy km s}^{-1}$  in the present images. A sum of the BIMA data over a  $22.5''$  box and over a  $300 \text{ km s}^{-1}$  range centered on the optical velocity of the galaxy gives an integrated flux of  $-5.6 \pm 6.0 \text{ Jy km s}^{-1}$ . If the CO detected by Sage & Wrobel (1989) was smoothly distributed over the  $225 \text{ km s}^{-1}$  velocity range and over the  $55''$  beam of the 12m telescope, it would be too faint to be detectable in the current interferometer images. Furthermore, it would be invisible to the interferometer, which does not sample those  $55''$  spatial scales. If, however, the CO detected by Sage & Wrobel (1989) was concentrated within one  $8'' \times 6''$  beam for each individual channel, it would have been detectable at the  $4\sigma$  to  $8\sigma$  level. Additional mosaic observations of NGC 4649 in BIMA's D configuration have better sensitivity to large scale structures; those observations will be reported in a future paper, and they also fail to detect CO in NGC 4649.

#### 4.2. CO fluxes and H<sub>2</sub> masses

For the galaxies with CO detections, total fluxes were measured from the integrated intensity images shown in figures 3, 8, 13, 18, and 23. The uncertainties in the CO fluxes are probably 10% for the stronger detections (NGC 3656, NGC 4476, and NGC 5666), dominated mostly by the absolute calibration. For NGC 807 and UGC 1503 the uncertainty is probably a bit larger, perhaps 15% to 20%, due to uncertainties in the absolute calibration and in choosing the spatial region to be summed.

The CO fluxes measured in the present images of UGC 1503, NGC 807, and NGC 4476 are consistent within 20% of the <sup>12</sup>CO 1-0 fluxes measured by WCH using the IRAM 30m telescope. WCH detected a larger CO flux from NGC 5666,  $60 \text{ Jy km s}^{-1}$ , than I find in the BIMA image ( $40 \text{ Jy km s}^{-1}$ ). The difference is nominally larger than the combined uncertainties, which are about 10% for the BIMA image and probably 10–15% for the data of WCH (C. Henkel, priv. comm.). However, there is no compelling evidence that the interferometer has missed a significant component of the molecular gas in this galaxy. Conversely, the images shown here reveal that the molecular gas distributions for UGC 1503, NGC 4476, and NGC 5666 are not very much larger than the  $23''$  (FWHM) beam of the 30m telescope, so there is no compelling evidence that the single dish spectra missed significant components of the molecular gas in these galaxies. The exception to this latter statement is NGC 3656, which has a factor of two larger flux in the BIMA images than in

the spectrum of WCH; most likely this is because the gas distribution is larger than the 30m beam. The CO line widths agree well in all cases.

H<sub>2</sub> masses (Table 4) are calculated using the distances in Table 1 and a “standard” H<sub>2</sub>/CO conversion factor of  $3.0 \times 10^{20} \text{ cm}^{-2} (\text{K km s}^{-1})^{-1}$  as in WCH. With this conversion factor, H<sub>2</sub> masses are related to CO fluxes  $S_{CO}$  by  $M(H_2) = (1.18 \times 10^4 M_\odot) D^2 S_{CO}$  where  $D$  is the distance in Mpc and  $S_{CO}$  is the CO flux in  $\text{Jy km s}^{-1}$ . No correction has been made for the presence of helium.

### 4.3. CO Morphology

Figures 3, 4, 8, 9, 13, 14, 18, 19, 23, and 24 show integrated CO intensity maps and channel maps for the five galaxies with detected CO emission. The molecular gas in these five elliptical galaxies is found in very regular, symmetric rotating disks with diameters of a few up to 12 kpc. The disks appear flat at the current resolution and sensitivity; the only feature which can be reliably identified outside of the flat disks is in NGC 3656 (Figure 13). In this galaxy, the majority of the molecular gas is found in a disk oriented north-south, following the optical dust lane (Balcells, van Gorkom, Sancisi, & del Burgo 2001). Roughly 6% of the galaxy’s total CO flux comes from a feature at  $11^h 23^m 40^s$ ,  $53^\circ 50' 20''$  (J2000), about  $10''$  west of the southern end of the main CO disk. The feature is also visible in the individual channel images (Figure 14) near  $2975 \text{ km s}^{-1}$ . The features above and below the disk of NGC 807 (Figure 8) may simply be noise.

With the current rather low resolution it is difficult to be sure whether the elongated molecular gas distributions come from disks or bars. I assume in the majority of this paper that they are disks because of the characteristic “butterfly” pattern which is apparent in the channel maps for UGC 1503, NGC 807, and NGC 4476 (Figures 4, 9, and 19). In this pattern, the channels near to the systemic velocity show gas distributions which are elongated in the direction of the kinematic minor axis but the edge channels show much more compact gas distributions. The pattern is characteristic of roughly circular gas disks inclined to the line of sight. NGC 807 and UGC 1503 also show rotation curves which rise and then flatten in the manner common to spiral galaxy gas disks (Section 4.4). The butterfly pattern is not obvious in the channel maps for NGC 3656 (Figure 14); I will continue to assume that the gas is in a disk rather than a bar, but higher resolution observations would be beneficial.

Two of the galaxies show evidence for asymmetries in their gas distributions (the CO emission is stronger on one side than the other). This effect is dramatic for NGC 807 (Figure 8), where approximately 30% of the CO emission comes from the northwest half of the galaxy and 70% from the southeast half. The asymmetry is also apparent in the channel maps of Figure 9, where the peak intensity in the channel at  $4880 \text{ km s}^{-1}$  is  $10\sigma$  but the peak intensity in the matching channels on the other side of the systemic velocity ( $4430$  and  $4480 \text{ km s}^{-1}$ ) is only  $5\sigma$ . Such a large intensity difference is unlikely to be due to noise. WCH’s spectrum of NGC 807 does not show the high velocity side to be stronger than the low velocity side, but this is probably because the

peak intensity in the  $4880 \text{ km s}^{-1}$  channel occurs  $10''$  away from the galaxy center (see also Figure 12). This means that the strongest emission in the galaxy comes from regions at the half power point of the IRAM 30m telescope beam, and the 30m telescope has much less sensitivity to this feature than the interferometer. A lopsided CO distribution is also evident in NGC 4476 (Figure 18), though to a lesser extent.

None of the galaxies show definitive evidence for CO at large radii as in Cen A (Charmandaris, Combes, & van der Hulst 2000). In that galaxy, at least 10% of the CO emission of the galaxy is not associated with the optical dust lane but is found in stellar shells at 15 kpc radius. The rms noise levels in the images (Table 2) are such that an unresolved source appearing in one channel at the  $5\sigma$  level would have a CO flux of 1 to 2  $\text{Jy km s}^{-1}$ , which is less than 10% of the CO fluxes of all of the galaxies detected here (Table 4). Thus, if 10% of the CO emission were in features like those of Cen A it would most likely have been detected. The numbers are particularly compelling for NGC 3656 (the galaxy which, optically, looks most disturbed). Molecular gas associated with the optical shell and containing as little as 1% of the total CO flux of that galaxy would probably have been detected. Thus, the present images suggest that Cen A is unique or at least unusual in having such large quantities of molecular gas associated with its shells.

In order to quantify the axis ratios and position angles of the CO distributions, the integrated intensity maps were fitted with elliptical Gaussians. The ellipticity and position angle of the fitted Gaussians are given in Table 4 along with estimates of the maximum detected extent of the CO.

#### 4.4. CO kinematics

Initial kinematic analysis of the molecular gas was performed by fitting simple solid body rotation profiles to the velocity fields in Figures 5, 10, 15, 20, and 25. NGC 807 and UGC 1503 were also fit with profiles that rise in their inner parts and then flatten. None of these fits constrain the disk inclination angles  $i$  or maximum rotation velocity particularly well; the product  $V \sin i$  is better constrained. But this procedure does give good estimates of the position angle of the kinematic major axis (Table 4), which were used for the position-velocity plots in figures 7, 12, 17, 22, and 27. Since the fits are weighted by the integrated intensity, the fitted angle is really the kinematic major axis at *small radii*. The only case in which the major axis clearly varies with radius is NGC 3656, which is described in more detail below.

Table 4 compares the morphological major axis described in section 4.3 to the kinematic major axis for each galaxy. In two cases (NGC 5666 and NGC 4476) the two axes are aligned to within a degree or so, well within the combined errors. In these galaxies all of the evidence is consistent with the molecular gas being in an intrinsically circular disk.

In one case (NGC 3656) there is a dramatic misalignment of nearly  $17^\circ$  between the two angles in Table 4, much larger than the combined errors of the fits. This misalignment is clearly visible in Figure 15 from the fact that the kinematic minor axis (the isovelocity curve at the systemic

velocity) is not perpendicular to the kinematic major axis at large radii or to the morphological major axis. However, the kinematic major axis at large radii does appear to be closely aligned with the morphological major axis. Thus, the molecular gas in NGC 3656 is either in a warped disk or is on elliptical orbits in a non-axisymmetric potential (Binney & Merrifield 1998). Optical images of this galaxy clearly show an S-shaped dust lane (e.g. Balcells, van Gorkom, Sancisi, & del Burgo (2001)) in which the twist of the dust lane is in exactly the sense needed to explain the twist in the CO kinematic major axis, so the CO probably follows the warped dust lane.

The remaining two cases (NGC 807 and UGC 1503) show moderate misalignments of  $6^\circ$  and  $12^\circ$  between the CO morphological and kinematic major axes. These misalignments are nominally greater than the uncertainties in the fits, but they are probably not reliable. These are the two galaxies for which the morphological position angles are the most questionable because the integrated intensity contours are the least elliptical.

The position-velocity diagrams show steeply rising, approximately solid body rotation regions in the center of each galaxy. In NGC 4476 and NGC 5666 the CO does not extend past the region of solid body rotation, which is at least three to four beams across. In NGC 3656 there are some signs that the CO rotation curve flattens near the edges of the CO distribution; note in particular the low-velocity side of the position-velocity diagram (Figure 17) and the velocity field (Figure 15). In NGC 807 and UGC 1503 (the most luminous galaxies of the sample, with the largest CO disk linear sizes) the rotation curve clearly turns over and becomes flat at radii of approximately 2.0 kpc (NGC 807) and 1.4 kpc (UGC 1503).

For these latter two galaxies whose rotation curves turn over, the kinematic centers of the gas are coincident with the optical centers of the galaxies (Cotton, Condon, & Arbizzani 1999) within an arcsecond or so (10% of the beam). For NGC 4476, NGC 3656, and NGC 5666 the kinematic centers are not well constrained, but the morphological centers of the molecular gas disks are closely coincident with the optical centers.

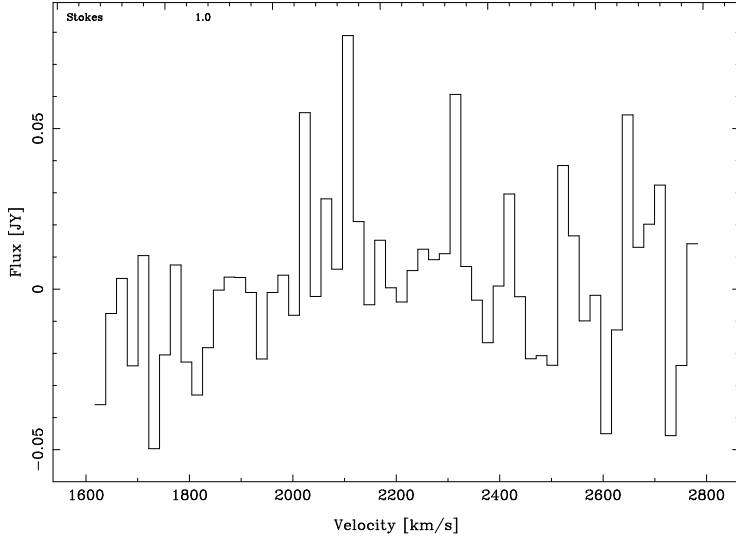


Fig. 1.— CO spectrum of a square region,  $22.5''$  on a side, centered on the optical center of NGC 7468.

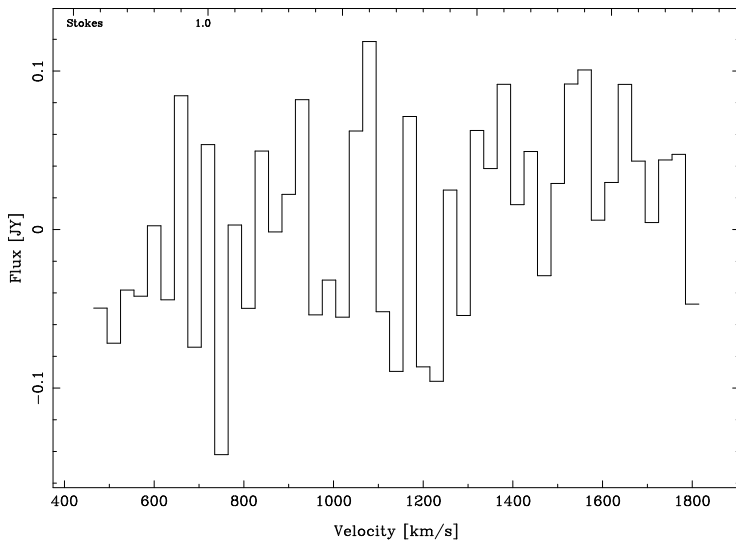


Fig. 2.— CO spectrum of a square region,  $22.5''$  on a side, centered on the optical center of NGC 4649.

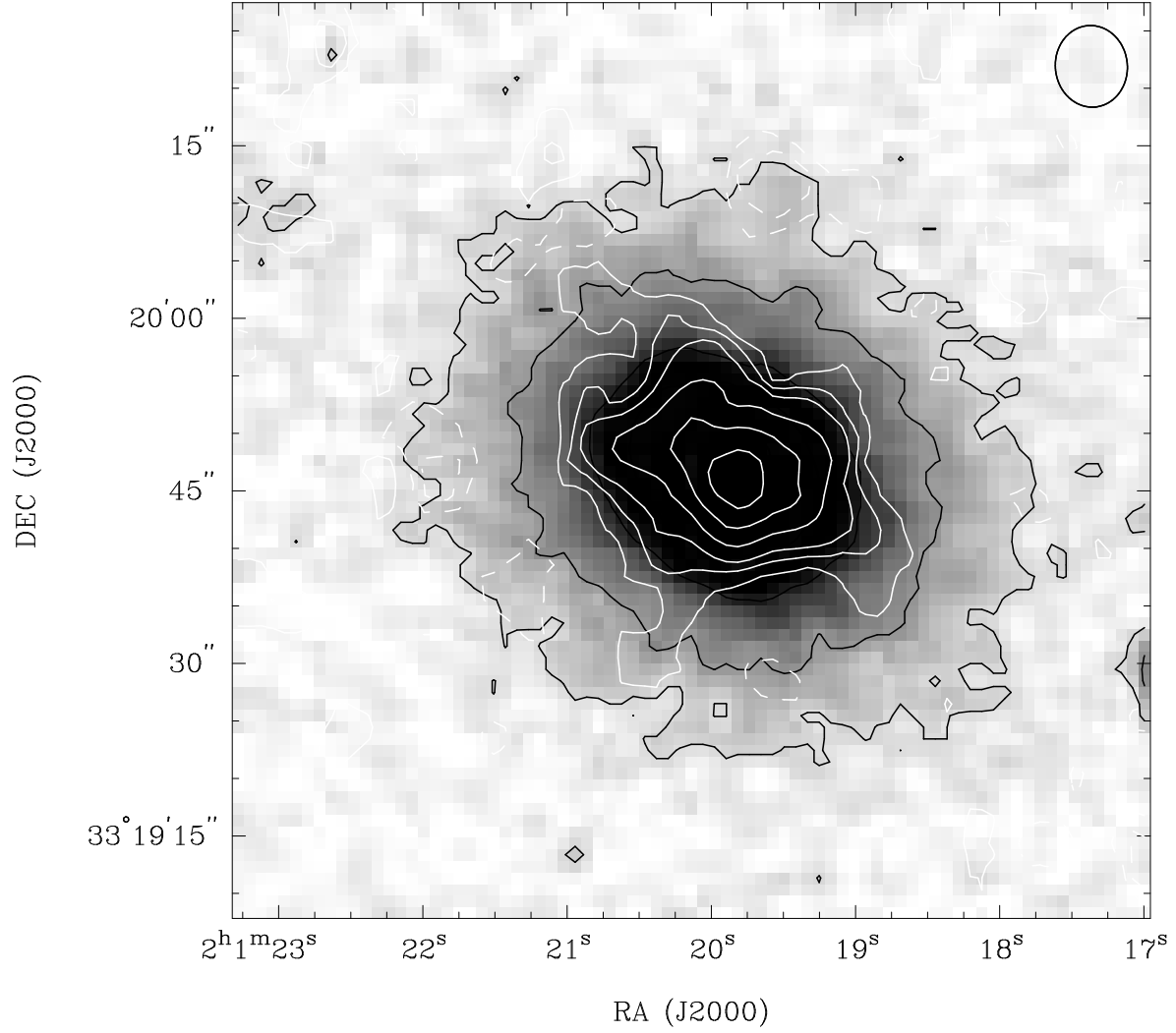


Fig. 3.— Molecular gas in UGC 1503. The greyscale and black contours are an optical image from the red portion of the second generation Digitized Sky Survey. The heavy white contours show the CO integrated intensity in units of  $-20$ ,  $-10$ ,  $10$ ,  $20$ ,  $30$ ,  $50$ ,  $70$ , and  $90$  percent of the peak, which is  $6.3 \text{ Jy b}^{-1} \text{ km s}^{-1} = 3.9 \times 10^{21} \text{ cm}^{-2}$  using the  $\text{H}_2/\text{CO}$  conversion factor described in Section 4.2. The small ellipse at the top indicates the size of the beam.

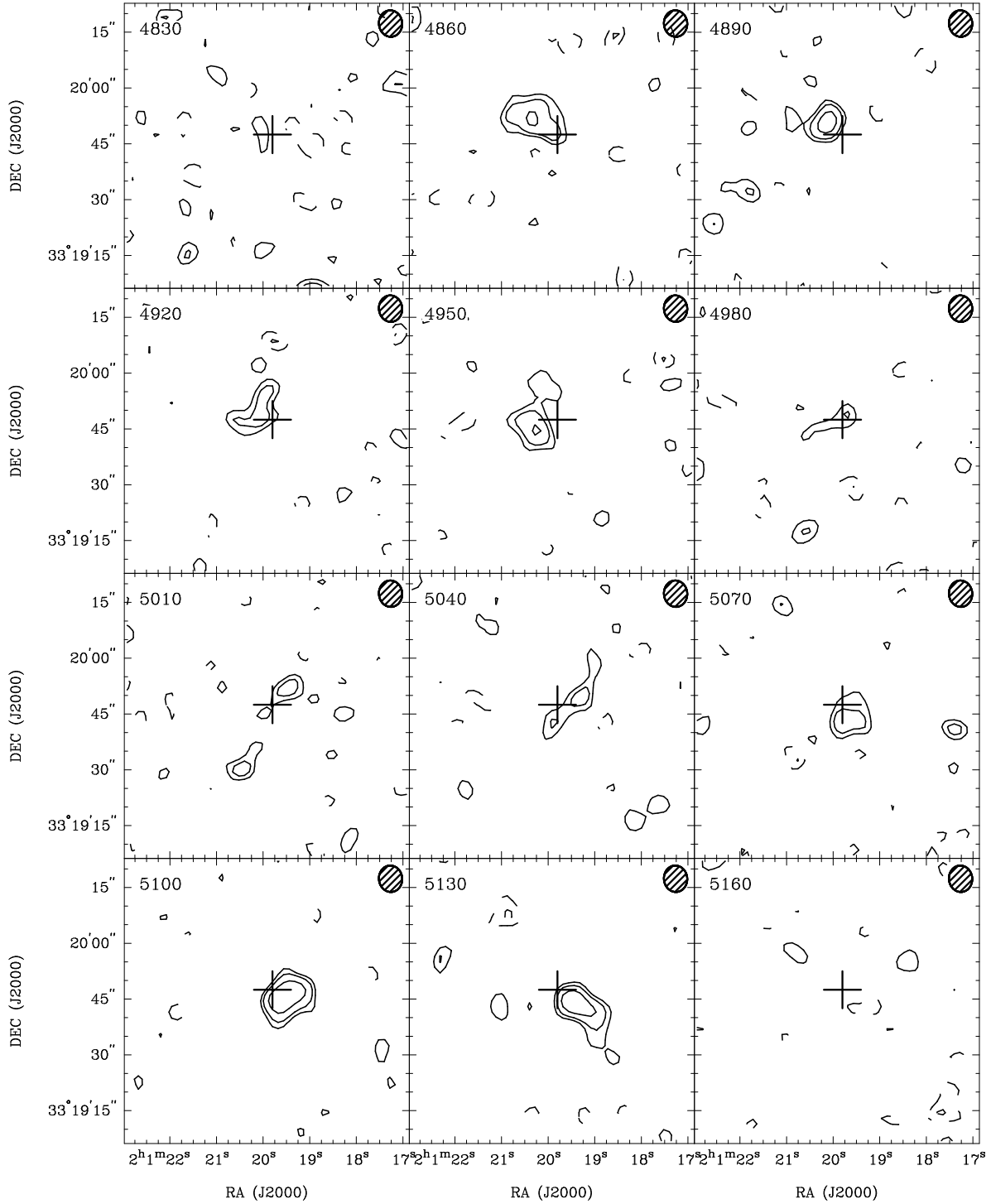


Fig. 4.— Individual channel maps showing CO emission from UGC 1503. Contour levels are  $-3, -2, 2, 3, 5, 8.3, 13.9,$  and  $23.1$  times  $8.0 \text{ mJy b}^{-1} \sim 1\sigma$ . The velocity of each channel (in  $\text{km s}^{-1}$ ) is indicated in the upper left corner and the beam size in the upper right corner. The cross marks the kinematic center of the gas, which coincides with the morphological center of the gas and the optical center to within  $1''$  to  $2''$ .



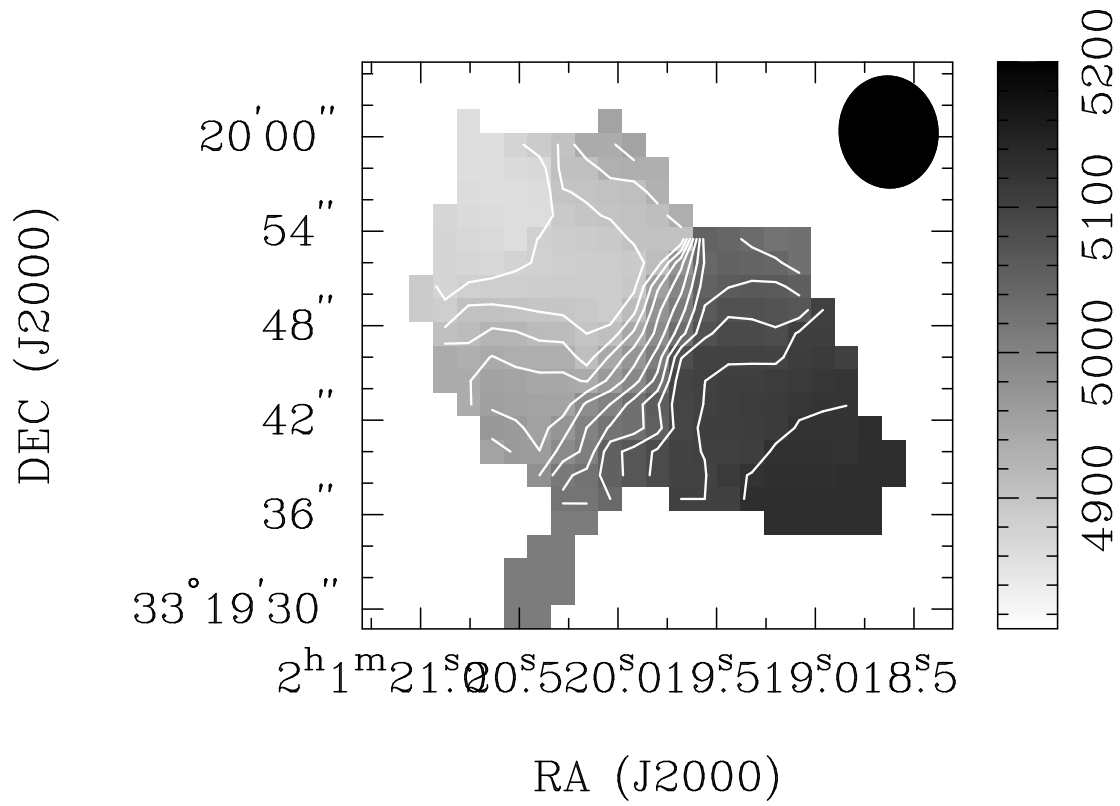


Fig. 5.— UGC 1503 velocity field. The CO intensity-weighted mean velocity (moment 1) is shown in grayscale and in contours from  $4860 \text{ km s}^{-1}$  to  $5120 \text{ km s}^{-1}$  in steps of  $20 \text{ km s}^{-1}$ . The ellipse shows the beam size.

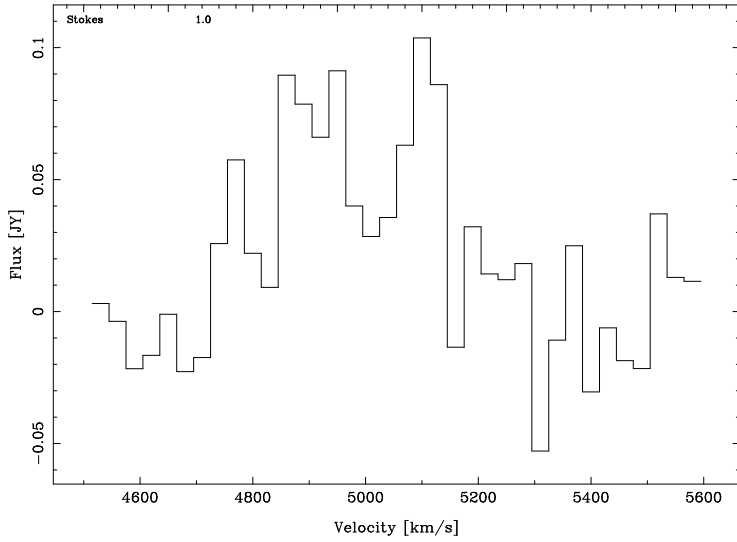


Fig. 6.— CO spectrum of UGC 1503. The spectrum was constructed by first using the integrated intensity image (Figure 3) to define an irregular mask region within which the emission is located. The intensity was integrated over the same spatial region for every channel, so the noise in the line-free regions of the spectrum should be indicative of the noise on the line as well.

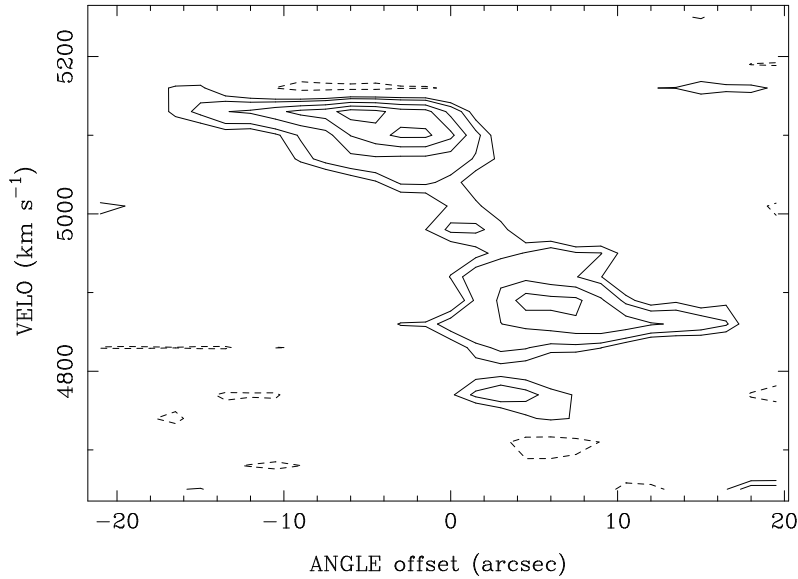


Fig. 7.— UGC 1503 position-velocity diagram. This slice is centered on the kinematic center of the molecular gas (RA=02 01 19.8, Dec=+33 19 47, J2000) and follows the kinematic major axis at  $-123^\circ$ . Contour levels are  $-20, 20, 30, 50, 70,$  and  $90$  percent of  $61.1 \text{ mJy b}^{-1}$ .

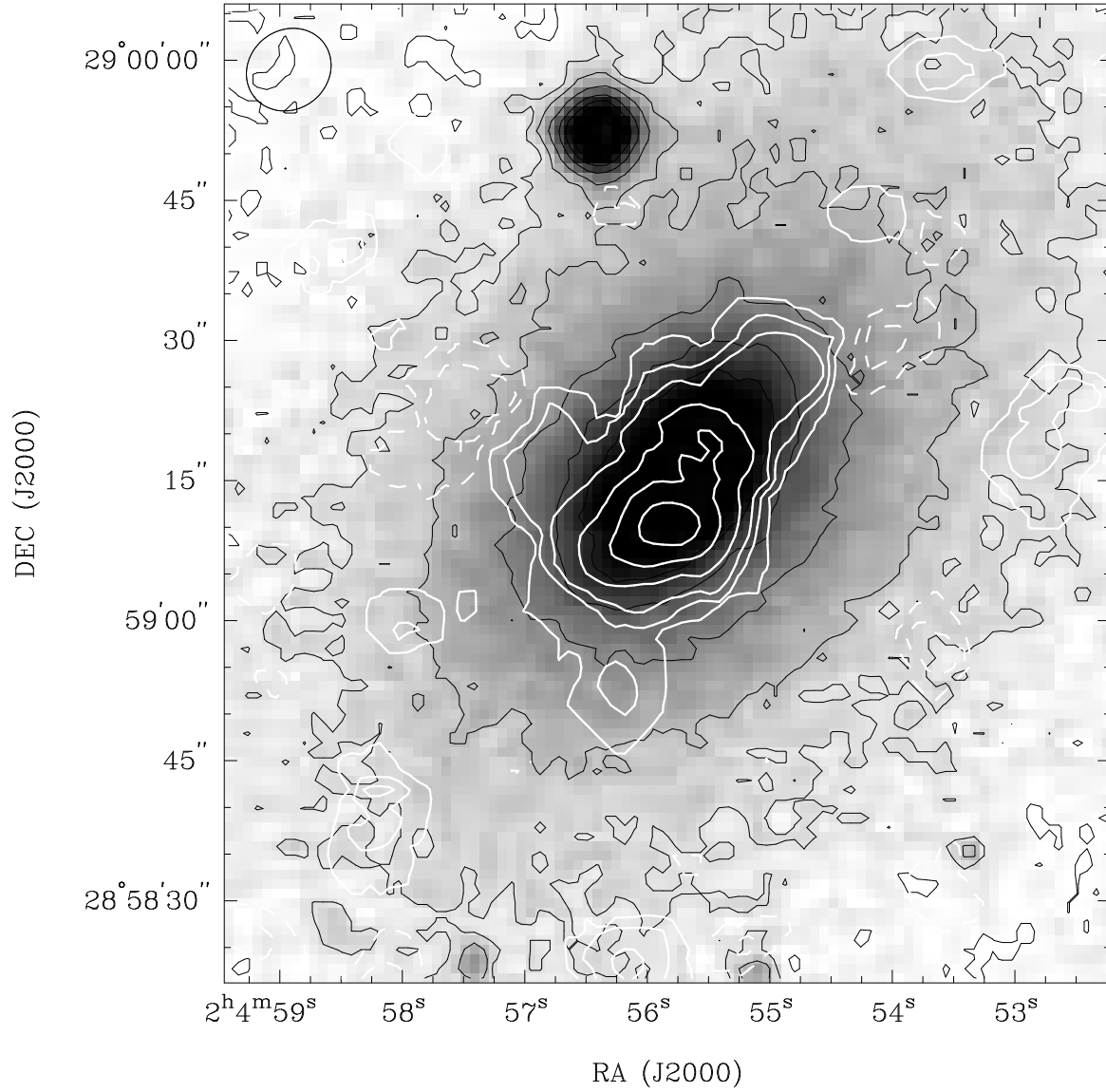


Fig. 8.— Molecular gas in NGC 807. Heavy white contours show the CO integrated intensity in units of  $-20$ ,  $-10$ ,  $10$ ,  $20$ ,  $30$ ,  $50$ ,  $70$ , and  $90$  percent of the peak ( $7.6 \text{ Jy b}^{-1} \text{ km s}^{-1} = 2.6 \times 10^{21} \text{ cm}^{-2}$ ). Other features as in Figure 3.

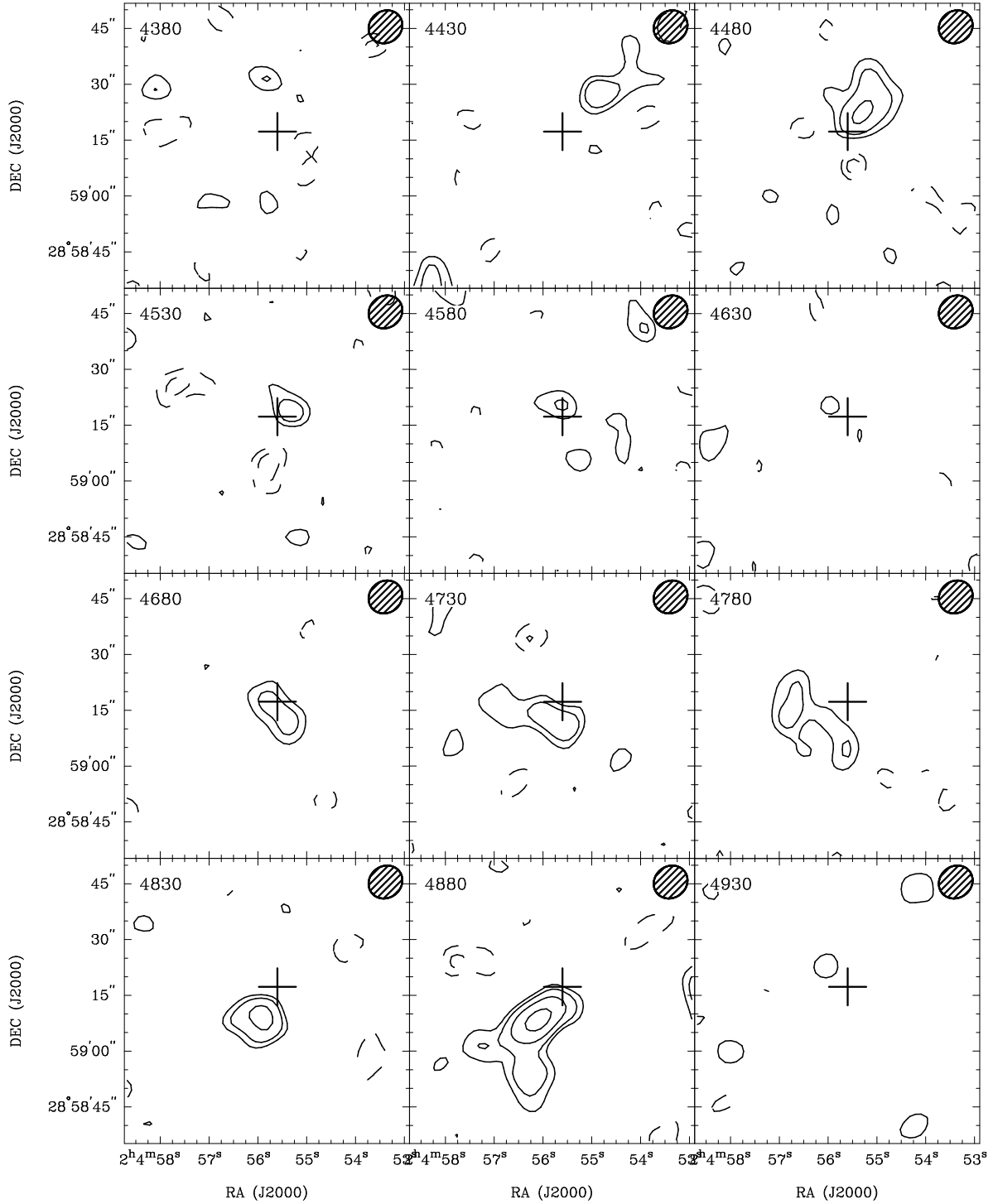


Fig. 9.— Individual channel maps showing CO emission from NGC 807. The contour intervals are the same as for Figure 4 but the multiplicative unit is  $1\sigma = 6.8 \text{ mJy b}^{-1}$ . The cross marks the kinematic center of the molecular gas; that location is coincident with the optical center of the galaxy, given the uncertainties (about  $2''$ ) in each position.

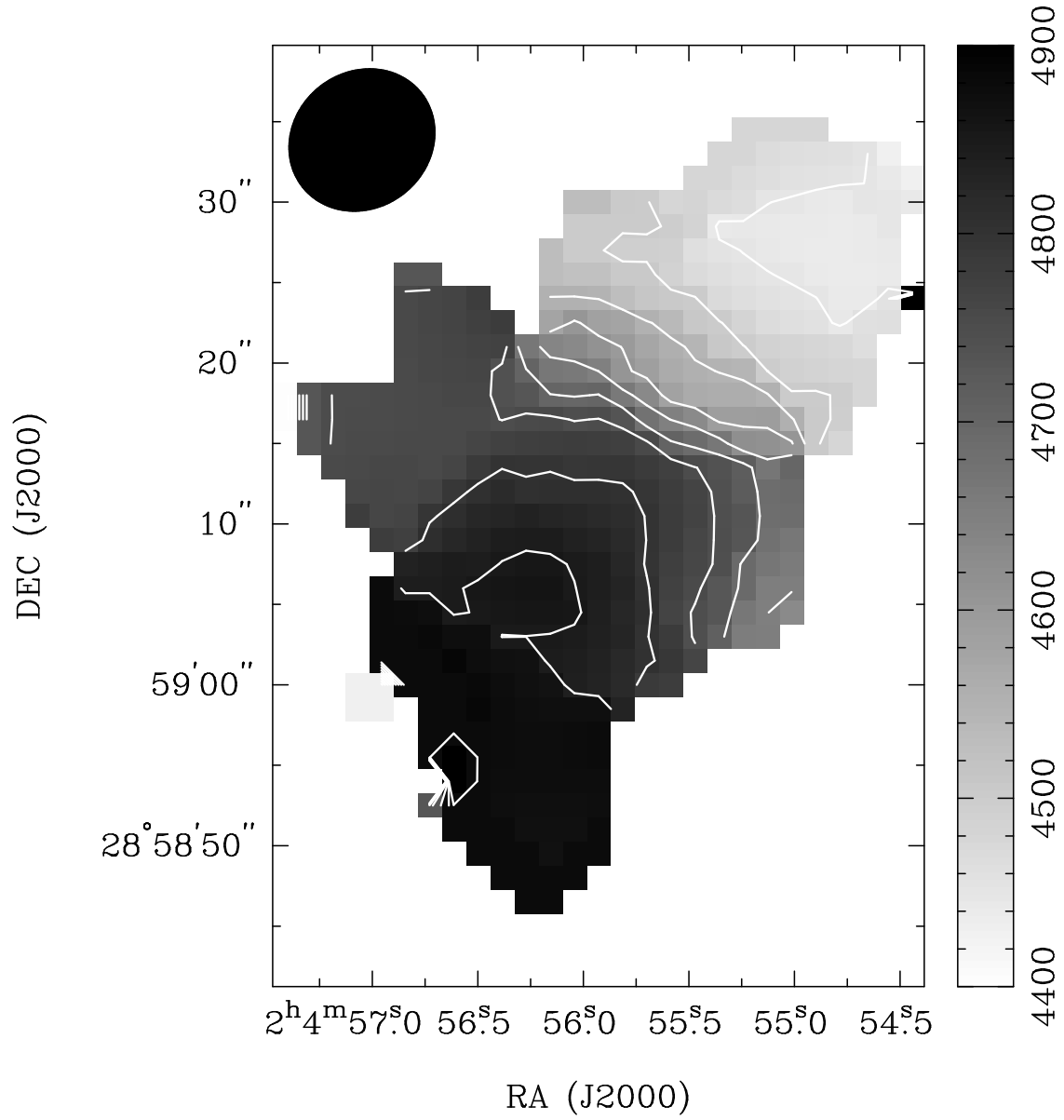


Fig. 10.— NGC 807 velocity field. The CO intensity-weighted mean velocity (moment 1) is shown in grayscale and in contours from  $4450 \text{ km s}^{-1}$  to  $4900 \text{ km s}^{-1}$  in steps of  $50 \text{ km s}^{-1}$ . The ellipse shows the beam size.

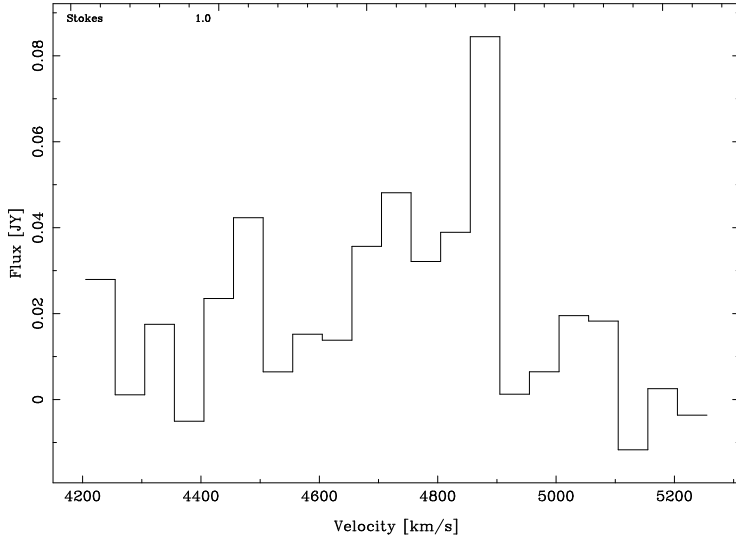


Fig. 11.— CO spectrum of NGC 807, constructed in the same manner as for Figure 6.

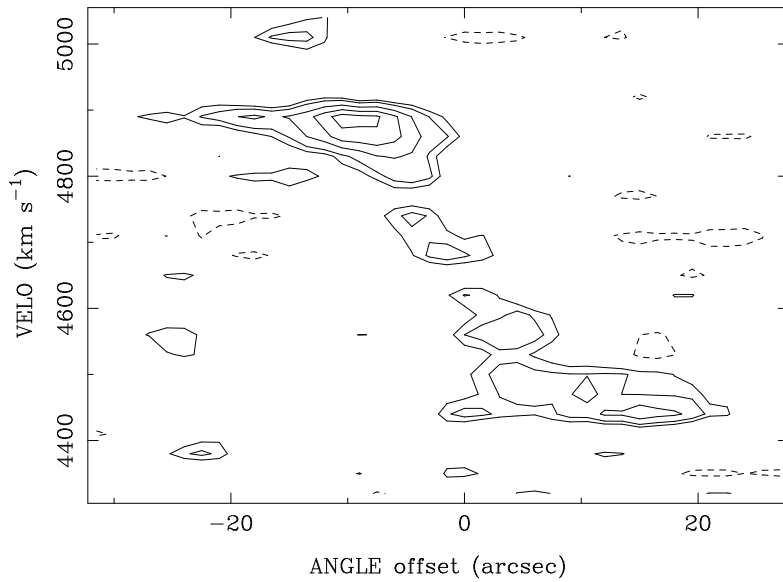


Fig. 12.— NGC 807 position-velocity diagram. This slice is centered on the kinematic center of the molecular gas (RA=02 04 55.6, Dec=+28 59 17, J2000) and follows the kinematic major axis at  $149^\circ$ . Contour levels are  $-20, 20, 30, 50, 70,$  and  $90$  percent of  $56.8 \text{ mJy b}^{-1}$ .

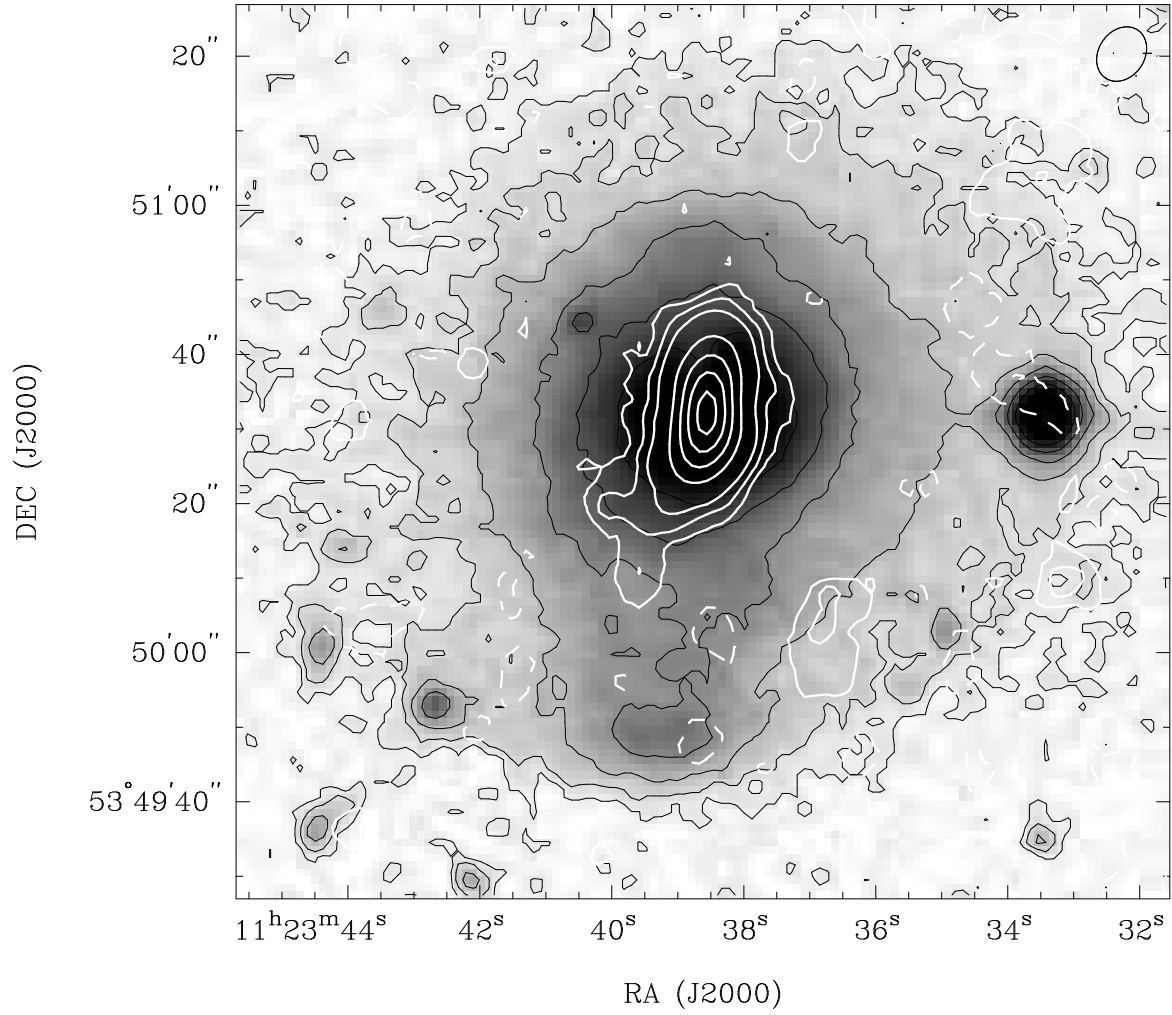


Fig. 13.— Molecular gas in NGC 3656. Heavy white contours show the CO integrated intensity in units of  $-5$ ,  $-2$ ,  $2$ ,  $5$ ,  $10$ ,  $20$ ,  $30$ ,  $50$ ,  $70$ , and  $90$  percent of the peak ( $81.1 \text{ Jy b}^{-1} \text{ km s}^{-1} = 4.7 \times 10^{22} \text{ cm}^{-2}$ ). Other features as in Figure 3.

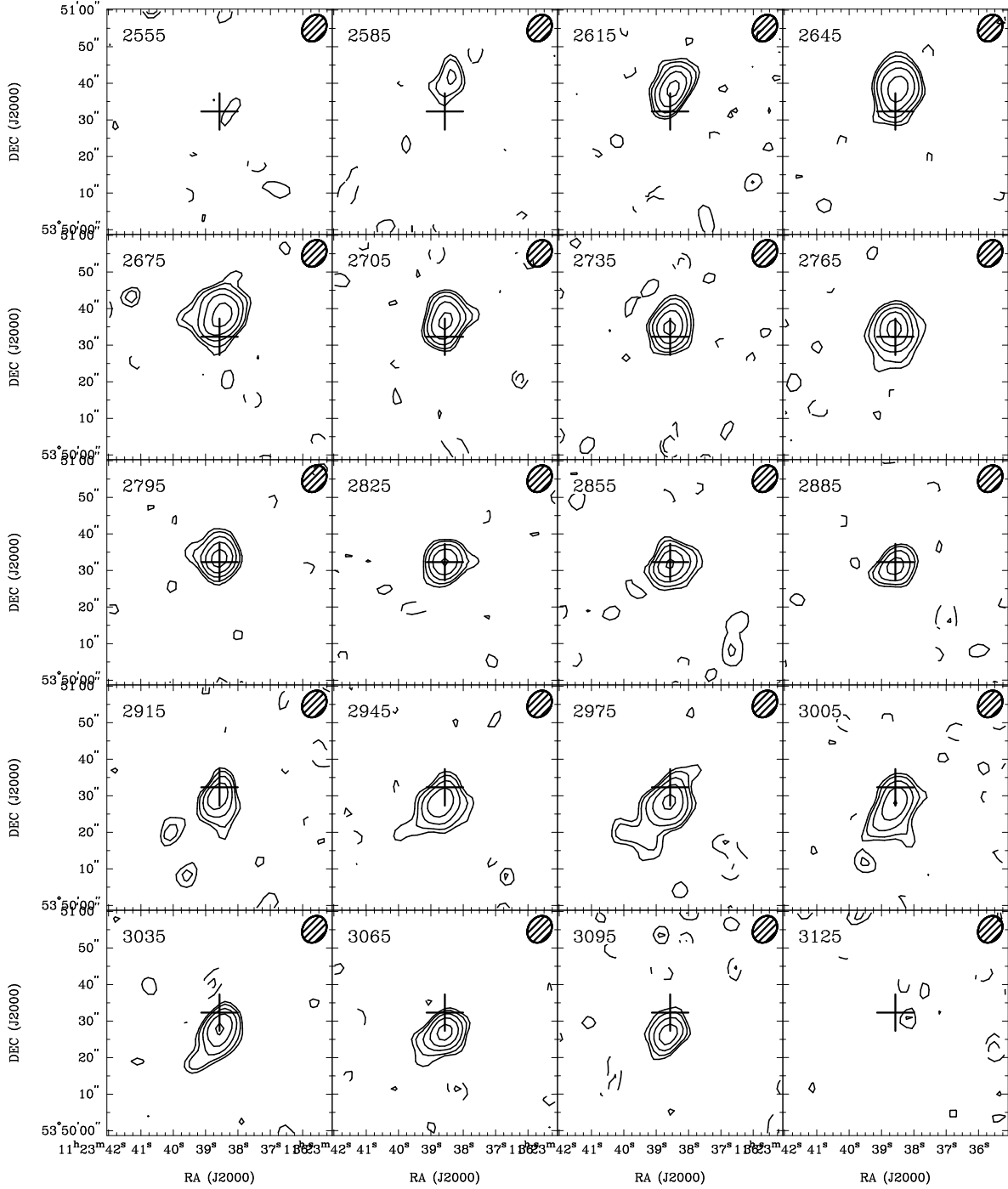


Fig. 14.— Individual channel maps showing CO emission from NGC 3656. As for Figure 4, but the contour levels are multiplied by  $1\sigma = 16 \text{ mJy b}^{-1}$ . The cross marks the morphological center of the molecular gas, which is coincident with the optical center to  $1''$ .



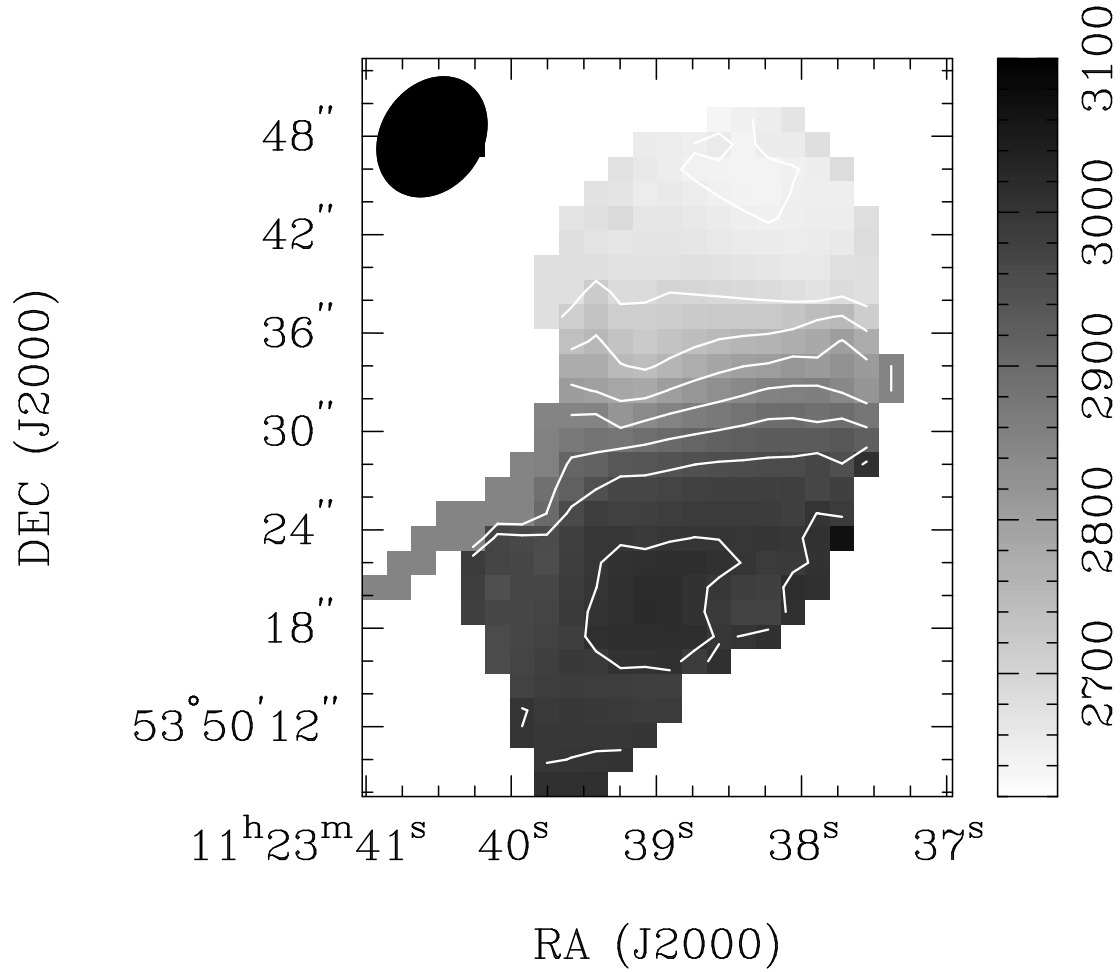


Fig. 15.— NGC 3656 velocity field. The CO intensity-weighted mean velocity (moment 1) is shown in grayscale and in contours from  $2650 \text{ km s}^{-1}$  to  $3000 \text{ km s}^{-1}$  in steps of  $50 \text{ km s}^{-1}$ . The ellipse shows the beam size.

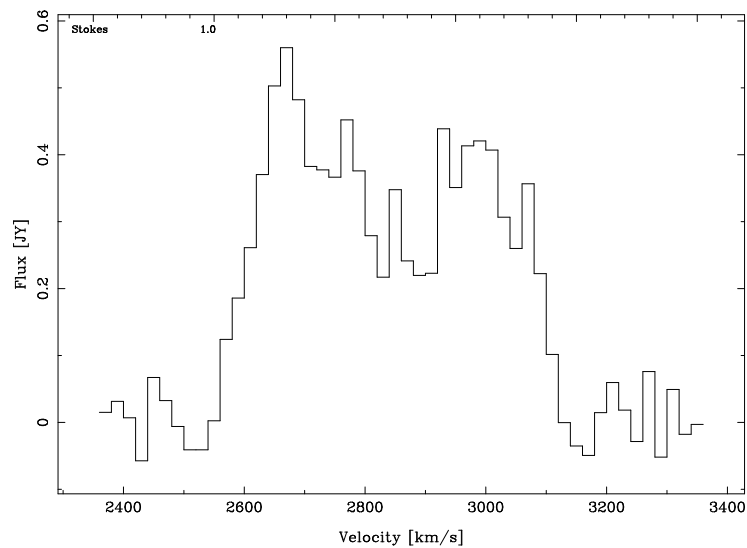


Fig. 16.— CO spectrum of NGC 3656, constructed in the same manner as for Figure 6.

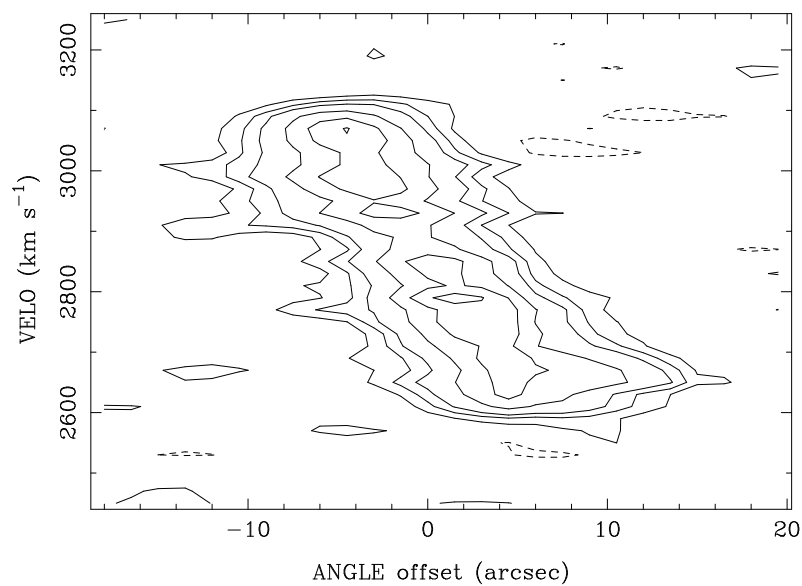


Fig. 17.— NGC 3656 position-velocity diagram. This slice is centered on the morphological center of the molecular gas (RA=11 23 38.57, Dec=+53 50 32.3, J2000) and follows the kinematic major axis at  $191^\circ$ . Contour levels are  $-20$ ,  $-10$ ,  $10$ ,  $20$ ,  $30$ ,  $50$ ,  $70$ , and  $90$  percent of  $292.7 \text{ mJy b}^{-1}$ .

#### 4.5. Dynamical Masses

These interferometric observations provide two important pieces of information that are missing from single-dish CO surveys of ellipticals: the linear sizes and axial ratios of the molecular disks. If the disks are assumed to be intrinsically circular, with gas on circular orbits, the inclination angle of the disk is given by  $i \geq \cos^{-1}(b/a)$  where  $b/a$  is the minor/major axis length ratio and the equality is achieved only in the limit that the disk is very thin. The observed gas velocities can then be used to calculate the dynamical mass interior to the disk’s outer edge:

$$M_{dyn} = (2.33 \times 10^5 M_{\odot}) V^2 R$$

where  $R$  is the radius of the outer edge in kpc and  $V$  is the observed velocity in  $\text{km s}^{-1}$ , corrected for inclination. The implied dynamical masses (Table 5) range from a few  $\times 10^9 M_{\odot}$  to nearly  $10^{11} M_{\odot}$  interior to the edge of the CO disk, and the observed masses of molecular gas are a few percent of these dynamical masses. Table 5 also gives the orbital time for gas at the edges of the CO disks.

#### 4.6. CO vs. stellar morphology

Optical images from the red plates of the second generation Digitized Sky Survey (DSS) were used in a comparison of CO and stellar morphologies. After sky subtraction, elliptical isophotes were fit to the optical images. The ellipticity, position angle, and center of each isophote were allowed to vary freely. The isophote fits are generally not good within a semi-major axis of  $5''$ , where the Sky Survey images are overexposed, or beyond  $30''$ , where the images are underexposed. The region from  $10''$  to roughly  $30''$  is comparable to the size of the CO disks, and that is the region I focus on here. A second round of fitting in which the ellipse centers were held fixed did not significantly change the results over this radius range. For comparison purposes, elliptical isophote fits were also performed on the J, H, and K images of NGC 4476 from the Two Micron All Sky Survey (2MASS) data. Isophote fits to NGC 3656 are more complicated because of the fine structure and the prominent dust lane, so the results of Balcells (1997) are used for that galaxy.

Table 6 gives the radius range over which the isophote fits are considered reliable, the mean ellipticity and position angle for each galaxy, and the dispersion about the mean for roughly 12 independently fitted annuli in that radius range. NGC 807, NGC 4476, and NGC 3656 are better described by  $r^{1/4}$  surface brightness profiles than by exponential profiles over the radius range in question. UGC 1503 and NGC 5666 are about equally well fit by either, though the reliable radius range for NGC 5666 is rather small. There is no evidence of position angle twist in any of the galaxies except for NGC 5666, which shows a  $10^\circ$  change in position angle at semi-major axes around  $15''$ . UGC 1503 shows no significant trend in ellipticity with radius, but the others do, and the dispersions about the mean ellipticities are determined mostly by the magnitude of those trends. The Sky Survey data for NGC 4476 give results which are consistent with those from the 2MASS data and the work of Simien & Prugniel (1997); my fits for UGC 1503 are consistent with those of Fasano & Bonoli (1989).

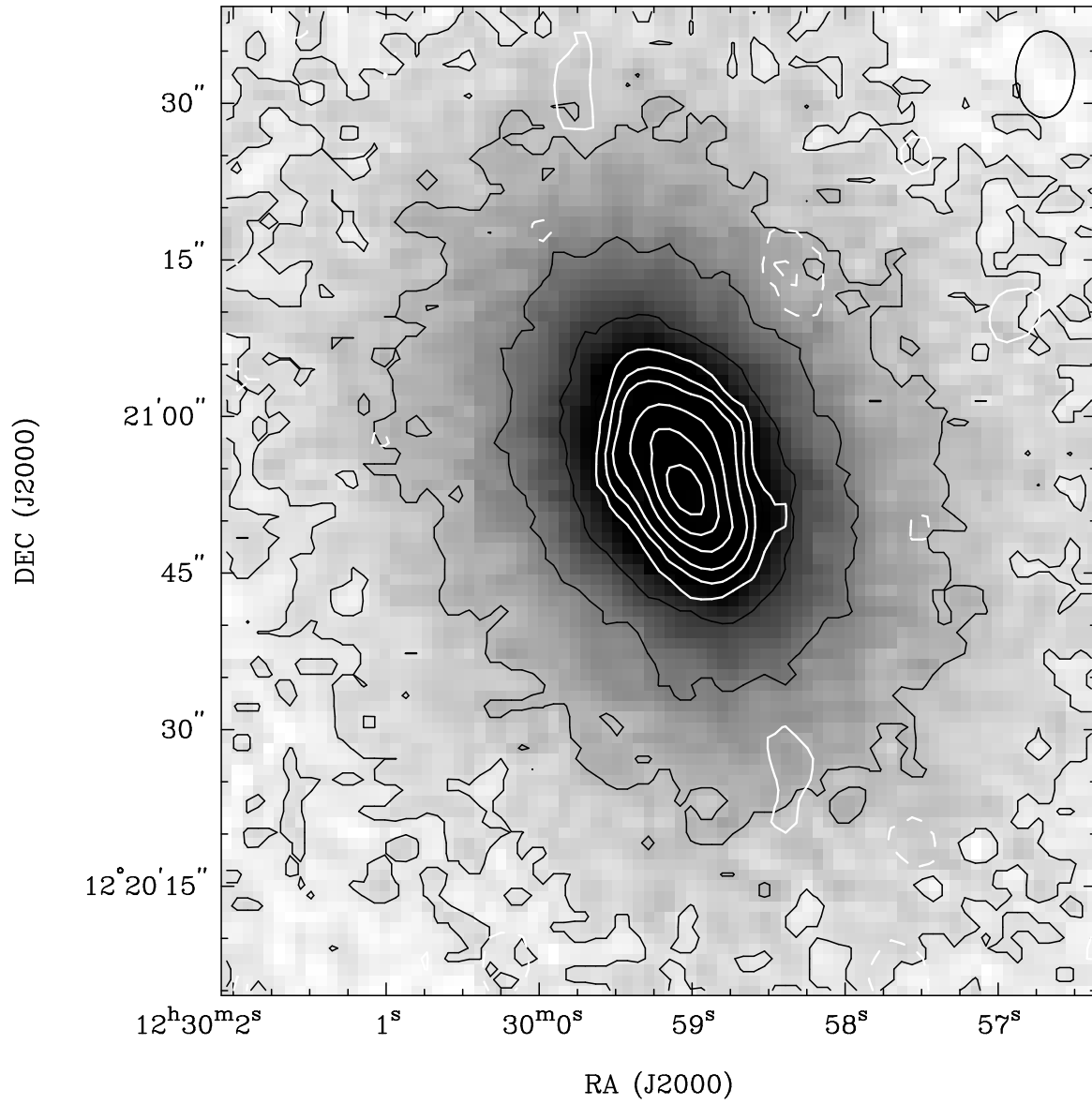


Fig. 18.— Molecular gas in NGC 4476. Heavy white contours show the CO integrated intensity in units of  $-20, -10, 10, 20, 30, 50, 70,$  and  $90$  percent of the peak ( $12.4 \text{ Jy b}^{-1} \text{ km s}^{-1} = 7.3 \times 10^{21} \text{ cm}^{-2}$ ). Other features as in Figure 3.

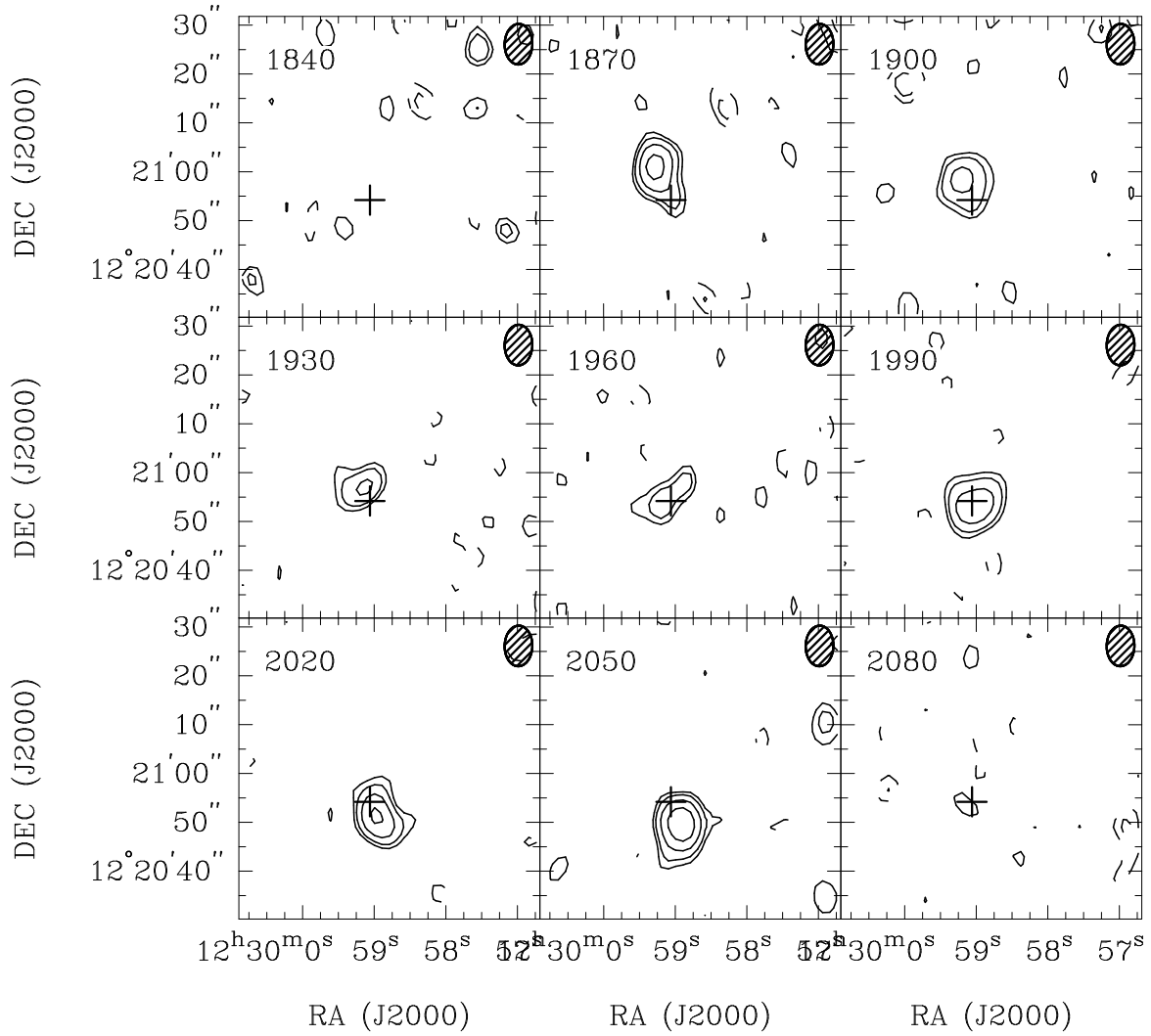


Fig. 19.— Individual channel maps showing CO emission from NGC 4476. As for Figure 4, but the contour levels are multiplied by  $1\sigma = 11.5 \text{ mJy b}^{-1}$ . The cross marks the morphological center of the gas, which is coincident with the optical center of the galaxy to about  $2''$ .

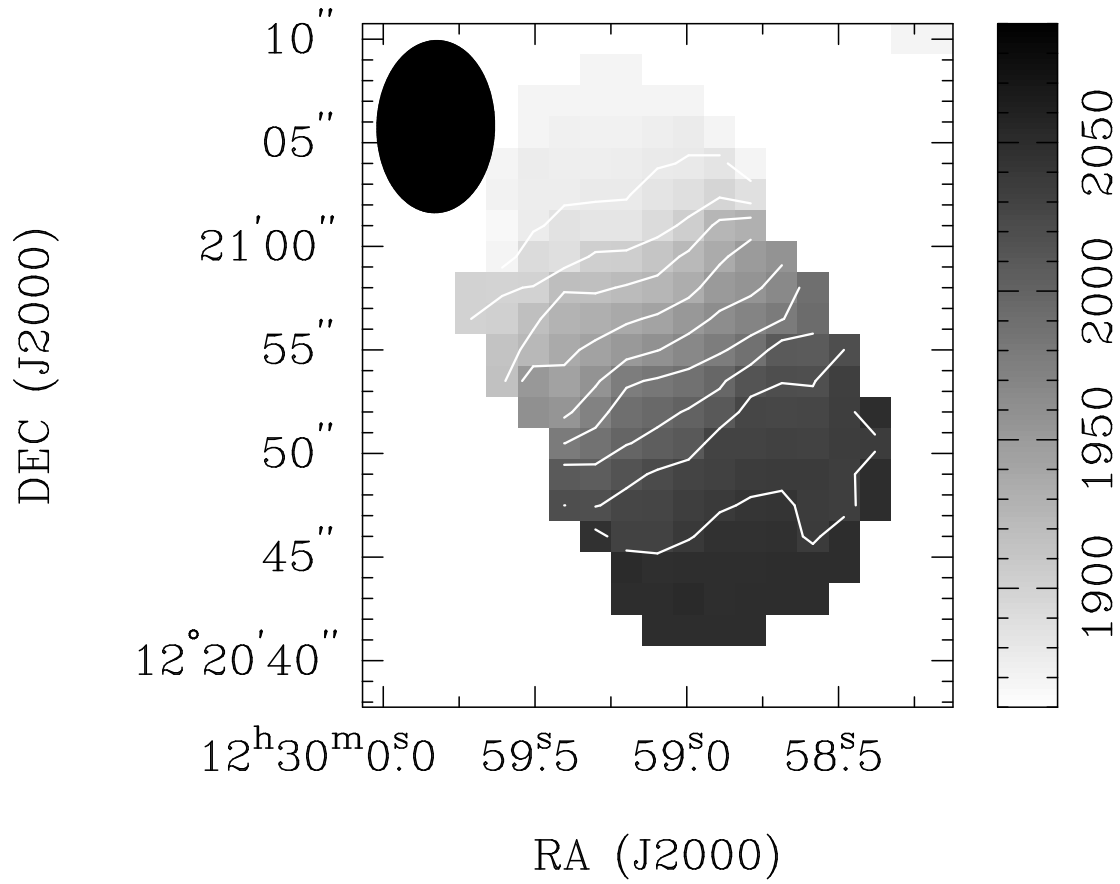


Fig. 20.— NGC 4476 velocity field. The CO intensity-weighted mean velocity (moment 1) is shown in grayscale and in contours from 1860 km s<sup>-1</sup> to 2040 km s<sup>-1</sup> in steps of 20 km s<sup>-1</sup>. The ellipse shows the beam size.

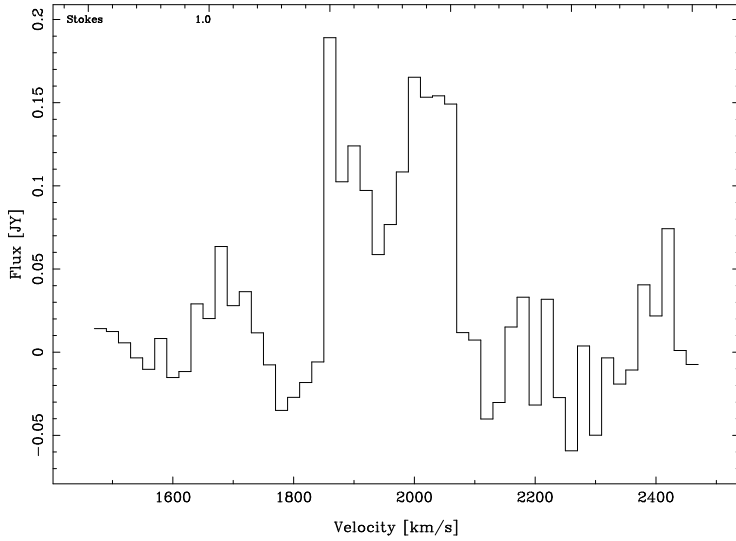


Fig. 21.— CO spectrum of NGC 4476, constructed in the same manner as for Figure 6.

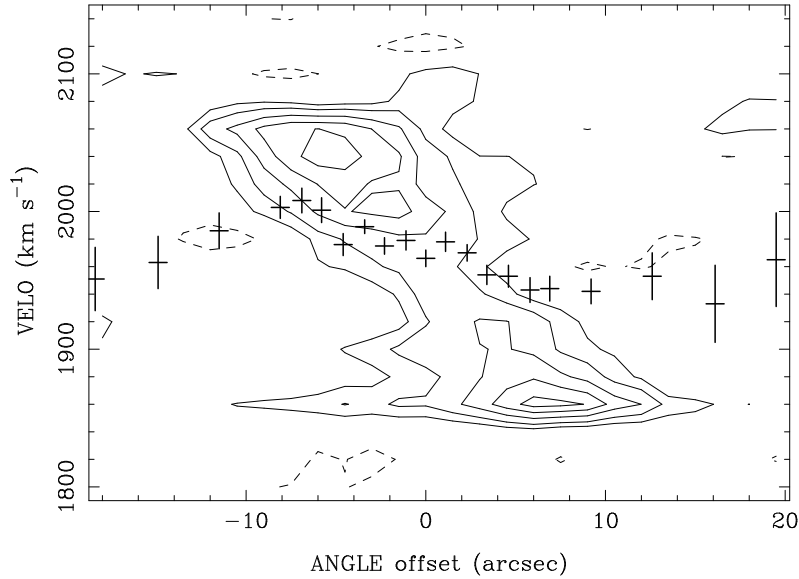


Fig. 22.— NGC 4476 position-velocity diagram. This slice is centered on the morphological center of the molecular gas (RA=12 29 59.06, Dec=+12 20 54.2, J2000) and follows the kinematic major axis at  $-152^\circ$ . Contour levels are  $-15, 15, 30, 50, 70,$  and  $90$  percent of  $125.1 \text{ mJy b}^{-1}$ . The crosses indicate stellar velocities measured along the major axis by Simien & Prugniel (1997); they have been uniformly shifted in velocity by  $12 \text{ km s}^{-1}$  to make the systemic velocity of the stars agree with that of the molecular gas. The difference between heliocentric velocities (in the stellar data) and LSR (in the CO) is  $4 \text{ km s}^{-1}$  at this position.

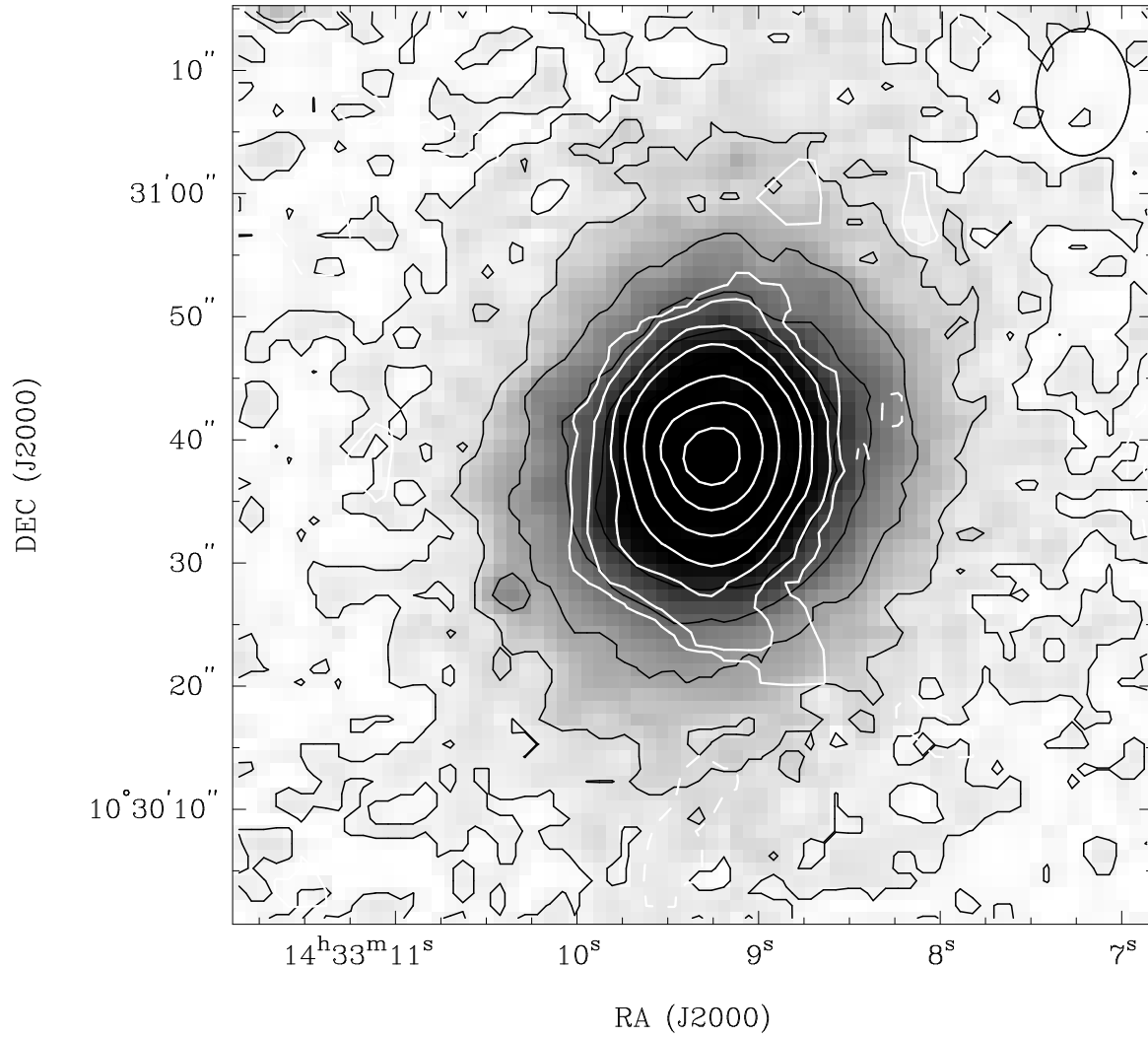


Fig. 23.— Molecular gas in NGC 5666. Heavy white contours show the CO integrated intensity in units of  $-10$ ,  $-5$ ,  $5$ ,  $10$ ,  $20$ ,  $30$ ,  $50$ ,  $70$ , and  $90$  percent of the peak ( $21.3 \text{ Jy b}^{-1} \text{ km s}^{-1} = 7.5 \times 10^{21} \text{ cm}^{-2}$ ). Other features as in Figure 3.



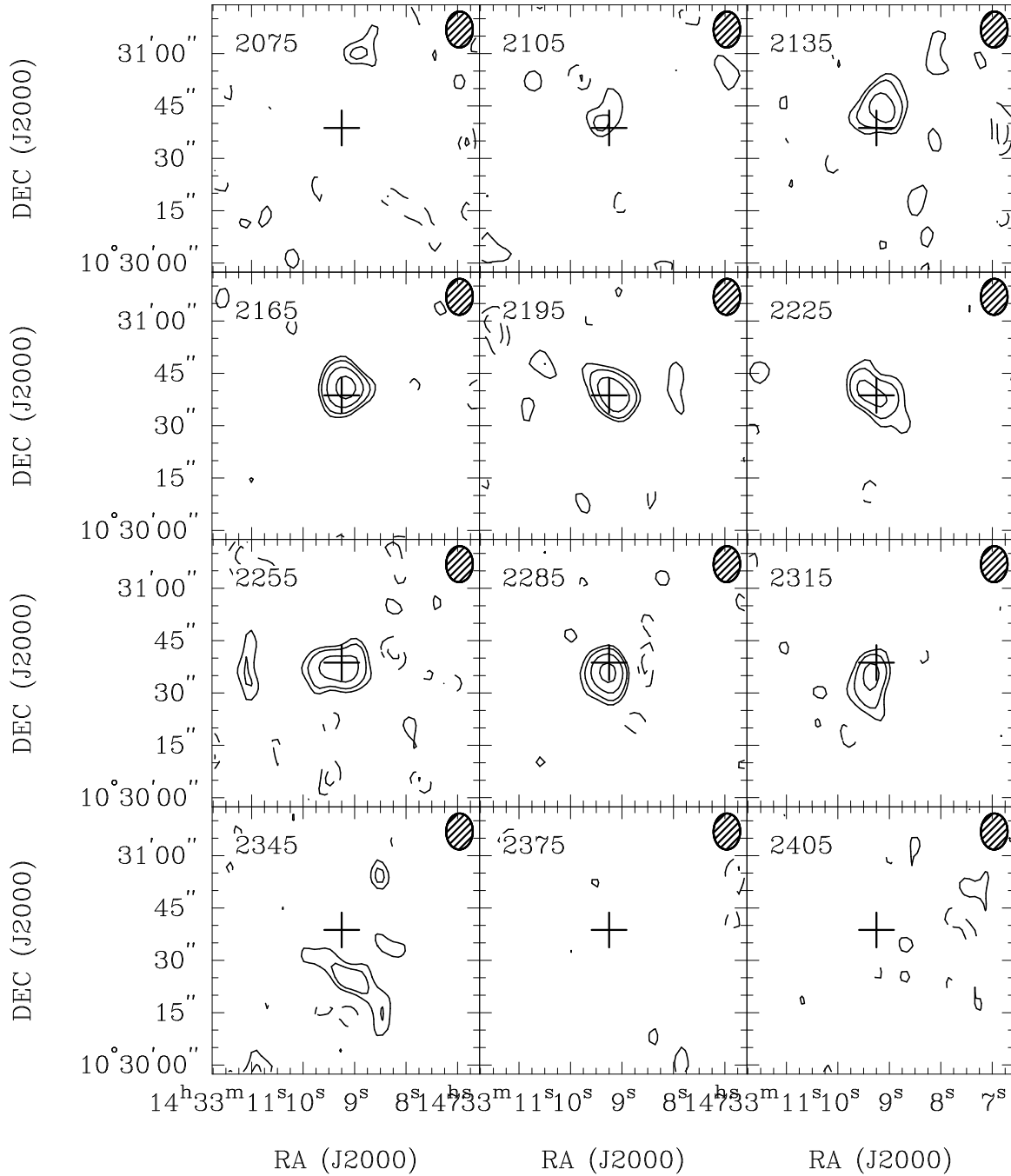


Fig. 24.— Individual channel maps showing CO emission from NGC 5666. As for Figure 4, but the contour levels are multiplied by  $1\sigma = 15 \text{ mJy b}^{-1}$ . The cross marks the morphological center of the molecular gas, which coincides with the optical center given in NED to better than  $1''$ .

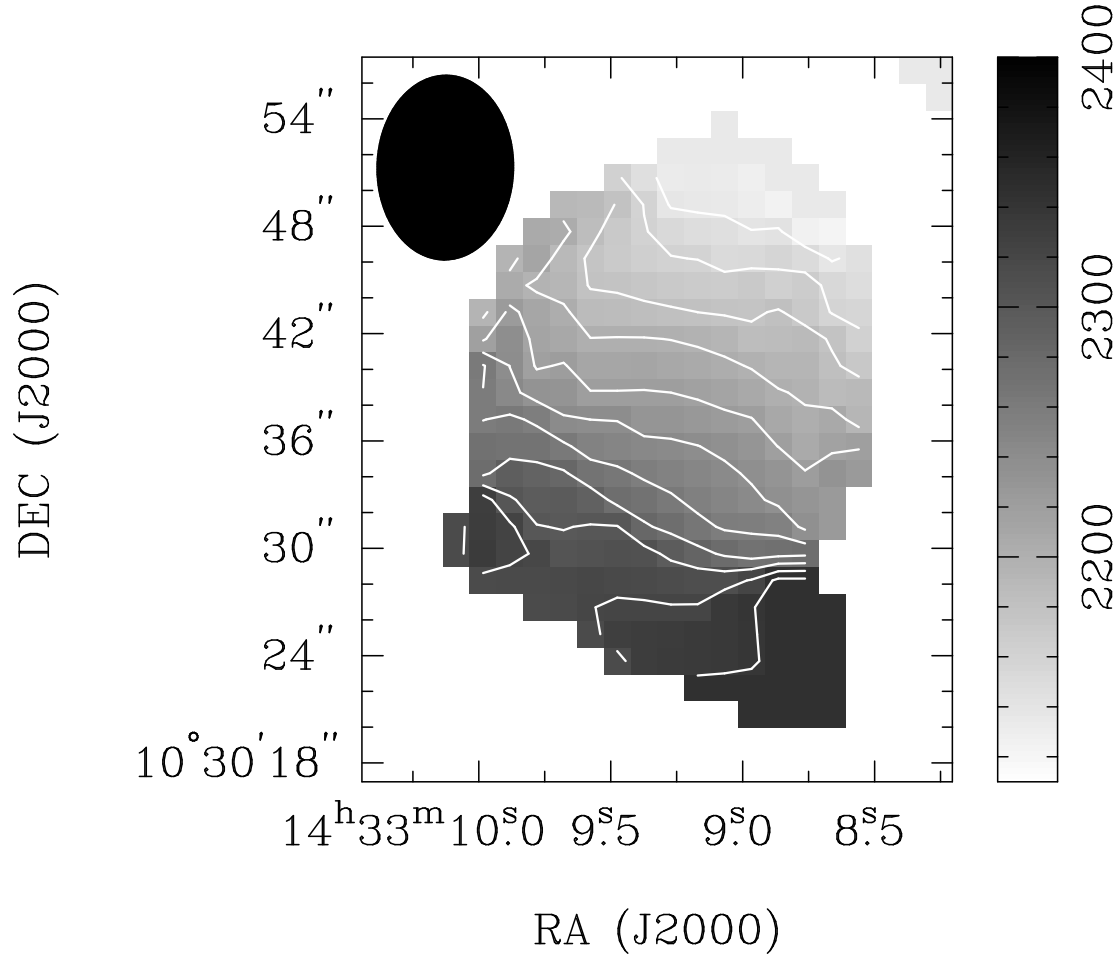


Fig. 25.— NGC 5666 velocity field. The CO intensity-weighted mean velocity (moment 1) is shown in grayscale and in contours from 2120 km s<sup>-1</sup> to 2340 km s<sup>-1</sup> in steps of 20 km s<sup>-1</sup>. The ellipse shows the beam size.

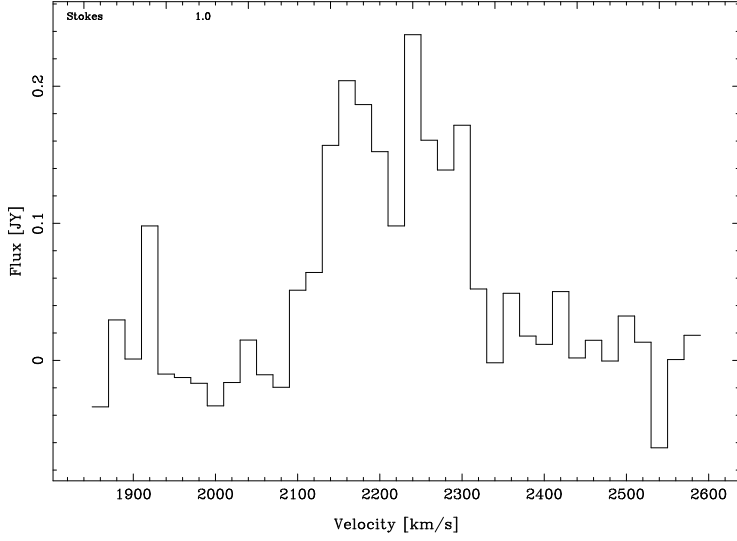


Fig. 26.— CO spectrum of NGC 5666, constructed in the same manner as Figure 6.

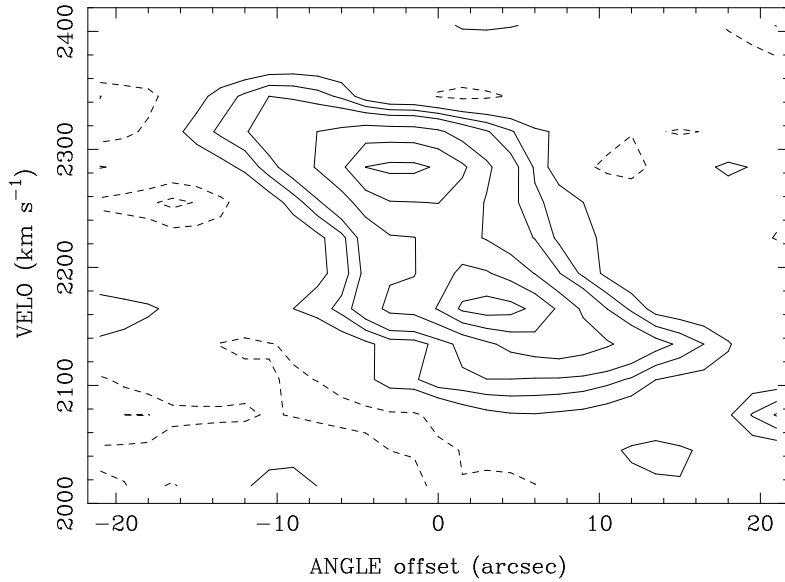


Fig. 27.— NGC 5666 position-velocity diagram. This slice is centered on the morphological center of the molecular gas (RA=14 33 09.25, Dec=+10 30 38.7, J2000) and follows the kinematic major axis at 165°. Contour levels are  $-20$ ,  $-10$ ,  $10$ ,  $20$ ,  $30$ ,  $50$ ,  $70$ , and  $90$  percent of  $149.7 \text{ mJy b}^{-1}$ .

The stellar isophotes are significantly rounder than CO isophotes, as one would expect in the case where the stars are dynamically hot and gas is dynamically cold. The only exception to this statement is NGC 5666, where the stars and the gas have equal ellipticities within the errors. Table 6 also gives the misalignment angle between the optical major axis and the CO kinematic axis; except for NGC 3656, which is close to a minor axis gas/dust disk, they are close to zero. In other words, four of the five galaxies have remarkably well-aligned (within  $13^\circ$ ) major axis gas disks.

## 5. Discussion

### 5.1. The origin of the molecular gas

Two ideas about the origin of molecular gas in ellipticals are (1) that the gas came from mass loss from the galaxy’s own evolved stars or (2) that the gas was acquired in an interaction or a merger with another gas-rich galaxy. In the second category I also include the idea that the molecular gas in ellipticals may simply be leftover from the formation of the elliptical, if ellipticals are formed by the merger of two roughly equal-mass spiral galaxies (Toomre & Toomre 1972). In the first model, internal stellar mass loss, Faber & Gallagher (1976) estimate that mass loss rates would be  $1.5 M_\odot \text{ yr}^{-1}$  per  $10^{11} L_\odot$  of optical luminosity. Over  $10^{10}$  years this gas would be comparable to the observed gas masses, at least within a factors of a few (the uncertainties in the  $\text{H}_2/\text{CO}$  conversion factor are at least factors of a few). The difficulty with this model is that the cold gas contents of elliptical galaxies are uncorrelated with their optical luminosities (Knapp, Turner, & Cuniffe 1985; Lees et al. 1991). Furthermore, the stellar mass loss is thought to be shock-heated by the stellar velocity dispersions to X-ray temperatures, and the hot plasma is thought to destroy dust grains on relatively short timescales (Wiklind & Henkel 2001).

The second idea, that the molecular gas in ellipticals has been acquired in a major or minor merger, may plausibly agree with the data presented here. Barnes (2002) has shown, *via* numerical simulations, that the merger of two gas-rich spiral galaxies produces systems which are qualitatively similar to the present sample of ellipticals and their gas disks. Some of the gas loses its angular momentum in shocks and falls to the nucleus of the galaxy, but up to 60% of the original gas contained in the spirals can form a rotationally supported gas disk with a radius of up to 20 kpc. Thus, the gas disks formed in these simulations are large enough to explain the observed gas disks (keeping in mind that the mass and size of the simulated disks are highly dependent on the geometry of the interaction). More careful analysis of the distribution and kinematics of the molecular gas in these ellipticals offers some important insight into these competing models and the origin of the molecular gas.

### 5.1.1. Gas and stellar kinematics

Figure 22 shows CO and stellar kinematics along the major axis of NGC 4476. The stellar kinematics are taken from Simien & Prugniel (1997), who also give a value of  $14.8''$  for the effective radius ( $r_e$ ) of this galaxy. The CO velocity rises linearly with radius to a maximum velocity of  $100 \text{ km s}^{-1}$  at  $7''$  radius. The stellar velocities also rise linearly with radius to a maximum rotation velocity of  $35 \text{ km s}^{-1}$  (3 times smaller than the CO velocity) at  $7''$  radius. Beyond  $7''$ , the stellar velocities appear to decline again so that there is little sign of rotation at  $r_e$ .

The stellar velocity dispersion is  $65 \pm 13 \text{ km s}^{-1}$  in the center of the galaxy, much larger than the stellar rotation velocities; the stars are primarily pressure-supported rather than rotationally supported. This means that the *stellar* rotation velocities in Figure 22 significantly underestimate the circular rotation speed of the galaxy (the asymmetric drift effect). The cold molecular gas probably gives a good indication of the circular speed. But the stellar rotation velocities *do* indicate the specific angular momentum of the stars. Within  $r_e$ , the specific angular momentum of the gas is about three times larger than that of the stars. Furthermore, if the observed trend in stellar rotation continues beyond  $r_e$ , then the stars in the outer parts of the galaxy also have very small specific angular momentum. If internal stellar mass loss had produced this molecular gas, one would expect the gas to have the same specific angular momentum as the stars, or perhaps smaller, and this is clearly not the case. The only way to reconcile the specific angular momenta of the gas and the stars is to suppose that they have very different inclinations to the line of sight, but that would again be unlikely if the gas originated in the stars. An external origin for the gas in NGC 4476 is strongly favored.

A similar situation seems to be true for NGC 3656. Balcells & Stanford (1990) obtained stellar kinematics along two position angles, both of which are  $50^\circ$  away from the CO major axis. They infer that the maximum stellar rotation velocity in the inner  $10''$  is on the order of  $50 \text{ km s}^{-1}$  and that the stellar rotation axis is very close to what is now known to be the CO rotation axis. The CO rotation velocity is  $270 \text{ km s}^{-1}$ , five times larger than that of the stars, but firm statements about the specific angular momenta of the stars and the gas are not possible in this case because the stellar rotation curve may still be rising at large radii. Similar comparisons of gas and stellar kinematics for the other galaxies in the sample will be vital for a broader understanding of the origin of the molecular gas in ellipticals.

### 5.1.2. Orientation of molecular gas and dust

There are two cases in the present sample for which published optical images clearly show that there is a very close correspondence between the dust and molecular gas distributions. These cases include NGC 3656, mentioned in section 4.4, and NGC 4476. Tomita et al. (2000) show that the dust in NGC 4476 is settled into a very regular, highly inclined disk of diameter  $20''$ ; the CO disk is also very regular, highly inclined, and has diameter  $27''$ . The other galaxies of the present sample

do not have good dust images in the literature and dust features are not visible in the Digitized Sky Survey images, so detailed comparisons of their dust *vs.* CO morphologies will require higher quality optical images.

As mentioned in section 5.1, the cold gas contents of ellipticals are unrelated to their optical luminosities, and this fact is usually interpreted as evidence of the gas’s external origin (Wardle & Knapp 1986; Lees et al. 1991). But the cold gas and dust *distribution* within an individual galaxy are clearly not independent of the stars. van Dokkum & Franx (1995) studied the orientations of dust features in HST images of ellipticals; they found that dust features with semimajor axes smaller than 250 pc are well aligned with the optical major axes of their host galaxies. More recent workers (Verdoes Kleijn, Baum, de Zeeuw, & O’Dea 1999; Martel, Turner, Sparks, & Baum 2000; Tran et al. 2001) classify dust features into two classes: (1) smooth, regular disks and (2) irregular lanes or filaments. They find that the disks are closely aligned with their host galaxies’ major axes whereas the lanes are randomly oriented. The interpretation which is common to all of these studies is that the dust has been acquired from an external source; the initial orientation of the dust features is random and their structure is irregular, but the dust gradually settles into the preferred plane of the galaxy and becomes a regular disk.

The close alignments between the CO disks and the optical major axes of the present sample are consistent with what is seen in the dust studies mentioned above, if the present sample of CO disks correspond to the older and more relaxed dust systems. Note, however, the curious fact (probably a selection effect) that the CO disks studied here are larger than the dust features seen by van Dokkum & Franx (1995), Verdoes Kleijn, Baum, de Zeeuw, & O’Dea (1999), and Tomita et al. (2000). Most of the dust features have diameters smaller than 2 kpc whereas only one of the CO disks (NGC 4476) is that small.

## 5.2. The shape of these galaxies

Many attempts have been made to infer the intrinsic shape distribution of elliptical galaxies from their optical photometry and kinematics, but the true shape distribution is still poorly known because it is model-dependent. Some ellipticals may be oblate, but it seems highly unlikely that *all* of them are (Khairul Alam & Ryden (2002); Bak & Statler (2000) and references therein). However, the preponderance of major axis disks in the present sample suggests that the majority of the sample galaxies are oblate. The principal plane of an oblate spheroid is perpendicular to the short axis, and this short axis always projects onto the apparent minor axis if the galaxy is axisymmetric (de Zeeuw & Franx 1989). Thus, a relaxed gas disk in an oblate galaxy should be aligned with the optical major axis.

At the present time it is not clear whether there is a discrepancy between the number of oblate ellipticals in the present sample and in the optical studies mentioned above. The number of elliptical galaxies with CO maps is still too small to confirm or reject the hypothesis that the

CO-sample has been drawn from the same parent population as the optical studies. But when the number of ellipticals with CO maps is significantly greater, it should prove interesting to investigate whether the amount of molecular gas in these galaxies is correlated with their intrinsic shape.

### 5.3. Star formation and the future of the molecular gas

Molecular gas is understood to be the raw material for star formation; the transformation of gas into stars will create rotationally supported stellar disks within these ellipticals. An estimate of the masses of the stellar disks can be obtained from Table 5, which shows that the molecular gas masses in the sample galaxies are a few percent of the dynamical masses within the edge of the CO disks. Comparing the masses of the stellar disks to the masses of the spheroidal stellar components depends on an assumption that the dynamical mass within the CO disk arises mostly from stars. This assumption is reasonable for the galaxy interiors.<sup>1</sup> It is also likely that not quite all of the gas will be transformed into stars. These assumptions imply that the stellar disks will have masses on the order of a percent of the total stellar mass in the galaxies— perhaps somewhat more, if some of the molecular gas has already been transformed into stars.

The stellar disks which are likely to form out of these molecular disks will be very similar to the stellar disks which are now known to be common at least in disky ellipticals. Scorza et al. (1998); Scorza & Bender (1995); Cinzano & van der Marel (1994), and others who have done detailed photometric and kinematic studies of ellipticals find that many ellipticals contain both the usual spheroidal component (a bulge) and a stellar disk. In this respect the ellipticals have structure which is qualitatively similar to spirals, but with much larger bulge/disk ratios (Kormendy & Bender 1996). Scorza et al. (1998) and Scorza & Bender (1995) found that the stellar disks inside ellipticals are rotationally supported; their sizes vary widely but are commonly on the order of  $r_e$ ; and their disk/bulge (luminosity) ratios are commonly a few percent up to 0.3. Presumably, smaller stellar disks may exist as well but are more difficult to detect. In short, after star formation ceases and the molecular gas is gone, the current sample of ellipticals will look much like known disky ellipticals.

The formation of a rotationally-supported stellar disk may already have happened in NGC 4476, where the stellar rotation appears to die out at the edge of the CO disk. I propose that careful kinematic analysis of that galaxy will show a small stellar disk of radius  $15''$  and circular rotation speed  $\sim 100 \text{ km s}^{-1}$  superposed on a largely non-rotating spheroidal population.

Interestingly, Naab & Burkert (2001) already predicted the existence of molecular gas disks in some ellipticals, at least in the scenario where ellipticals are formed by the merger of two similar-

---

<sup>1</sup>For NGC 4476, the effective radius  $14.8''$  quoted by Simien & Prugniel (1997) is similar to the  $13''$  maximum radius of the CO (Table 4); the CO disk extends to approximately  $r_e$ . The other sample galaxies do not have published effective radii, but from Figures 3, 8, 13, and 23 it seems unlikely that the CO extends to radii much larger than  $r_e$ .

mass disk galaxies. They found that purely collisionless mergers of disk galaxies do not reproduce the detailed kinematics of real elliptical galaxies (see also Bendo & Barnes (2000)). In particular, the collisionless mergers do not have broad retrograde and steep prograde wings in the stellar line-of-sight velocity distributions, and those are the signatures of rotationally supported stellar disks. Therefore, Naab & Burkert (2001) suggested that real ellipticals with stellar disks must have *first* contained gas disks similar to the ones which are shown here; the gas disks later turned into stellar disks.

#### 5.4. Stability of the Asymmetries in NGC 807

The strong asymmetry in the CO distribution of NGC 807 (Section 4.3) is striking, particularly in view of the fact that the gas should be sheared by differential rotation on very short timescales. Figure 12 shows that the rotation curve for NGC 807 becomes flat at a distance of about  $6''$  (2.0 kpc) from the kinematic center of the galaxy. The peak of the CO distribution is about  $9''$  (2.8 kpc) from the center, well within the differentially rotating part of the galaxy. The orbital timescale at the farthest edge of the CO disk in NGC 807 is  $1.5 \times 10^8$  yr (Table 5), and the orbital timescale at the turnover point is only  $5 \times 10^7$  yr. These numbers are not strongly dependent on the assumed inclination, as the  $\sin i$  correction is only 10% for the CO in NGC 807 (Table 5).

Thus, the effects of differential rotation should have been severe for this gas over the last  $10^8$  or few  $\times 10^8$  years. It is difficult to understand how the strong asymmetry (twice as much emission from the southern half of the galaxy as from the northern half) could be maintained for as long as  $10^9$  years. One possible solution to the problem is that the gas was acquired less than  $10^9$  years ago. On the other hand, an interaction with another galaxy less than  $10^9$  years ago should leave other traces as well— features like shells, ripples, or tails in the optical or HI images, but none have been seen (Oosterloo, Morganti, & Sadler 1999; Dressel 1987).

There are several other possible solutions to this short timescale for shearing. For example, the molecular gas may be much farther from the center than it appears. The orbital timescale would then be longer than  $1.5 \times 10^8$  yr. This scenario implies a highly nonuniform distribution of molecular gas, which again might be evidence that the gas was acquired from some outside source. The molecular gas could be on elliptical orbits; the gas distribution should then show a peak in the place where the orbital speed is small. It is also possible that the peak in the CO intensity reflects not a peak in the total gas density but rather a change in the phase from atomic to molecular; comparisons with the atomic gas distribution could address this latter possibility.

One final way to avoid the shearing problem is if the molecular gas which peaks about  $9''$  south of the galaxy center (Figures 8 and 12) is strongly self-gravitating. This feature has a CO flux of  $9.2 \text{ Jy km s}^{-1}$ , so its mass (not including helium) is approximately  $4.5 \times 10^8 M_{\odot}$ . The mass and the fact that it is not well resolved in the spatial dimension are consistent with  $\text{H}_2$  densities in the range  $10^2$  to  $10^3 \text{ cm}^{-3}$  ( $4 \times 10^{-22}$  to  $4 \times 10^{-21} \text{ g cm}^{-3}$ , including helium), which are typical



values for Galactic giant molecular clouds. From the rotation velocity of the CO we infer that the galaxy itself has a mass of  $4.1 \times 10^{10} M_{\odot}$  within 2.8 kpc of the center, giving an average density of  $3.0 \times 10^{-23} \text{ g cm}^{-3}$ . In these conditions the Roche limit for molecular gas of density  $10^2$  to  $10^3 \text{ cm}^{-3}$  is 1.3 to 2.8 kpc, which implies that the molecular gas is quite close to the borderline between tidal instability and stability. Again, the molecular gas may be farther from the center than it appears, which would tend to increase its stability.

### 5.5. A cautionary note

Given that there are still only a very small number of ellipticals whose CO distribution has been mapped, it is important to remember that the CO distributions in the present sample may not be representative of ellipticals in general. For example, the galaxies have been selected from single-dish surveys which usually only made one pointing towards the center of each galaxy. Any ellipticals in which molecular gas avoids the inner  $10''$  (in radius) would not have been selected. Furthermore, the galaxies are selected to be bright at  $100 \mu\text{m}$ , but it is well known that IRAS is much more sensitive to warm dust than to cold dust. Ellipticals whose dust is primarily cold would also not have been selected. If interactions increase the FIR luminosity of a galaxy, the present sample may be biased towards galaxies that have recently undergone an interaction. Future progress in understanding the evolution of ellipticals requires some exploration of these kinds of selection effects.

## 6. Summary

Six elliptical galaxies from the CO survey of Wiklind, Combes, & Henkel (1995) and one from Sage & Wrobel (1989) were observed with the BIMA and OVRO millimeter arrays at about  $8'' \times 6''$  resolution (0.7 to 2 kpc). Five of the seven (UGC 1503, NGC 807, NGC 3656, NGC 4476, and NGC 5666) were detected and their CO emission is resolved into very regular rotating disks. The disk radii are 1 to 6 kpc and rotation velocities are 100 to  $280 \text{ km s}^{-1}$ ; orbital timescales at the edge of the disks are around  $10^8 \text{ yr}$ .

Two of the five detected galaxies have CO rotation curves which rise linearly and then flatten at radii of 1–2 kpc. Two other galaxies' rotation curves keep rising to the edge of the CO disk; one may flatten just at the outer edge of the CO. The sizes, observed velocities, and inclination angles of the disks enable robust dynamical mass estimates which range from  $3 \times 10^9 M_{\odot}$  for NGC 4476 to  $10^{11} M_{\odot}$  for NGC 807. Of course, the dynamical mass estimates pertain to the mass interior to the edge of the CO disk, which for NGC 4476 is about one effective radius. The  $\text{H}_2$  masses are only a few percent of the dynamical masses.

Four of the CO disks are aligned within  $13^\circ$  of their host galaxies' optical major axes. The high proportion of major axis gas disks suggests that these ellipticals are oblate. The exception,

NGC 3656 (a merger remnant), has a gas and dust disk nearly aligned with its minor axis. The kinematics of the gas in NGC 3656 show clear evidence for a warp, but the others do not appear to be warped at the current resolution and sensitivity.

In one case, NGC 4476, major axis stellar kinematics are available from the literature. The stars show some rotation over the radial range where the CO exists, but outside that range the stellar rotation velocity appears to drop to zero. The gas has a factor of three or so larger specific angular momentum than the stars, which strongly suggests that the gas in NGC 4476 has come from an external source rather than from internal stellar mass loss. However, the present analysis offers no insight into the question of whether the gas in NGC 4476 is leftover from a major merger or was acquired in a minor merger/interaction. The CO disks are well within the size range of the gas disks which are created in spiral-spiral merger simulations (Barnes 2002), so the major merger hypothesis is plausible in this respect. Only one of the galaxies shows clear evidence of a major merger (NGC 3656; Balcells (1997); Balcells, van Gorkom, Sancisi, & del Burgo (2001)).

If the molecular gas in these galaxies forms stars, it will make rotationally supported stellar disks with radii of a few kpc. These stellar disks will probably contain on the order of a percent of the total stellar mass. The disks will be very similar in character to the stellar disks which are now known in many ellipticals (Scorza et al. 1998), though perhaps somewhat less luminous than the stellar disks which are detectable at the present time.

Thanks to Michael Rupen for helping to get this project off the ground. Thanks to Tom Statler and the referee, C. Henkel, for helpful comments. Thanks also to the Berkeley-Illinois-Maryland Association and the Owens Valley Radio Observatory (both operated with support from the National Science Foundation) for generous investments of telescope time. The Digitized Sky Surveys were produced at the Space Telescope Science Institute under U.S. Government grant NAG W-2166. This publication also makes use of data products from the Two Micron All Sky Survey, which is a joint project of the University of Massachusetts and the Infrared Processing and Analysis Center, funded by the National Aeronautics and Space Administration and the National Science Foundation. This research has made use of the NASA/IPAC Extragalactic Database (NED) which is operated by the Jet Propulsion Laboratory, California Institute of Technology, under contract with the National Aeronautics and Space Administration. Last but not least, this work has been supported by National Science Foundation grant AST 00-74709.

## REFERENCES

- Akeson, R. 1998, BIMA memo series #68  
Bak, J. & Statler, T. S. 2000, *AJ*, 120, 110  
Balcells, M. 1997, *ApJ*, 486, L87

- Balcells, M., & Stanford, S. A. 1990, *ApJ*, 362, 443
- Balcells, M., van Gorkom, J. H., Sancisi, R., & del Burgo, C. 2001, *AJ*, 122, 1758
- Barnes, J. E. 2002, *MNRAS*, submitted (astro-ph/0201250)
- Bendo, G. J. & Barnes, J. E. 2000, *MNRAS*, 316, 315
- Binney, J. & Merrifield, M. 1998, *Galactic astronomy* (Princeton, NJ : Princeton University Press), pp. 513, 713–715
- Braine, J., Wyrowski, F., Radford, S. J. E., Henkel, C., & Lesch, H. 1995, *A&A*, 293, 315
- Charmandaris, V., Combes, F., & van der Hulst, J. M. 2000, *A&A*, 356, L1
- Cinzano, P., & van der Marel, R. P. 1994, *MNRAS*, 270, 325
- Colbert, J. W., Mulchaey, J. S., & Zabludoff, A. I. 2001, *AJ*, 121, 808
- Cotton, W. D., Condon, J. J., & Arbizzani, E. 1999, *ApJS*, 125, 409
- Cretton, N., Rix, H.-W., & de Zeeuw, P. T. 2000, *ApJ*, 536, 319
- de Zeeuw, T., & Franx, M. 1989, *ApJ*, 343, 617
- Dressel, L. L. 1987, *IAU Symp. 127: Structure and Dynamics of Elliptical Galaxies*, 127, 423
- Faber, S. M. & Gallagher, J. S. 1976, *ApJ*, 204, 365
- Fasano, G., & Bonoli, C. 1989, *A&AS*, 79, 291
- Gordon, M. A. 1991, *ApJ*, 371, 563
- Horellou, C., Black, J. H., van Gorkom, J. H., Combes, F., van der Hulst, J. M., & Charmandaris, V. 2001, *A&A*, 376, 837
- Huchtmeier, W. K., Sage, L. J., & Henkel, C. 1995, *A&A*, 300, 675
- Inoue, M. Y., Kamenno, S., Kawabe, R., Inoue, M., Hasegawa, T., & Tanaka, M. 1996, *AJ*, 111, 1852
- Khairul Alam, & Ryden, B. 2002, *ApJ*, in press (astro-ph/0201435)
- Kormendy, J., & Bender, R. 1996, *ApJ*, 464, L119
- Knapp, G. R., Guhathakurta, P., Kim, D., & Jura, M. A. 1989, *ApJS*, 70, 329
- Knapp, G. R. & Rupen, M. P. 1996, *ApJ*, 460, 271
- Knapp, G. R., Turner, E. L., & Cunniffe, P. E. 1985, *AJ*, 90, 454

- Lay, O. 1999, BIMA memo series # 72
- Lees, J. F., Knapp, G. R., Rupen, M. P., & Phillips, T. G. 1991, *ApJ*, 379, 177
- Martel, A. ;, Turner, N. J., Sparks, W. B., & Baum, S. A. 2000, *ApJS*, 130, 267
- Naab, T. & Burkert, A. 2001, *ApJ*, 555, L91
- Oosterloo, T., Morganti, R., & Sadler, E. 1999, *PASA*, 16, 28
- Padin, S., Scott, S. L., Woody, D. P., Scoville, N. Z., Seling, T. V., Finch, R. P., Giovanine, C. J., & Lawrence, R. P. 1991, *PASP*, 103, 461
- Prugniel, P., Nieto, J.-L., & Simien, F. 1987, *A&A*, 173, 49
- Quillen, A. C., de Zeeuw, P. T., Phinney, E. S., & Phillips, T. G. 1992, *ApJ*, 391, 121
- Regan, M. W., Thornley, M. D., Helfer, T. T., Sheth, K., Wong, T., Vogel, S. N., Blitz, L., & Bock, D. C.-J. 2001, *ApJ*, 561, 218
- Reuter, H-P., Pohl, M., Lesch, H., & Sievers, A. W. 1993, *A&A*, 277, 21
- Rydbeck, G., Wiklind, T., Cameron, M., Wild, W., Eckart, A., Genzel, R., & Rothermel, H. 1993, *A&A*, 270, L13
- Sage, L. J., & Wrobel, J. M. 1989, *ApJ*, 344, 204
- Sault, R. J., Teuben, P. J., & Wright, M. C. H. 1995, in *ASP Conf. Ser. 77, Astronomical Data Analysis Software and Systems IV*, ed. R. A. Shaw, H. E. Payne, & J. J. E. Hayes (San Francisco: ASP), 433
- Scorza, C., Bender, R., Winkelmann, C., Capaccioli, M., & Macchetto, D. F. 1998, *A&AS*, 131, 265
- Scorza, C., & Bender, R. 1995, *A&A*, 293, 20
- Scoville, N. Z., Carlstrom, J. E., Chandler, C. J., Phillips, J. A., Scott, S. L., Tilanus, R. P. J., & Wang, Z. 1993, *PASP*, 105, 1482
- Simien, F., & Prugniel, Ph. 1997, *A&AS*, 122, 521
- Tomita, A., Aoki, K., Watanabe, M., Takata, T., & Ichikawa, S. 2000, *AJ*, 120, 123
- Toomre, A. & Toomre, J. 1972, *ApJ*, 178, 623
- Tran, H. D., Tsvetanov, Z., Ford, H. C., Davies, J., Jaffe, W., van den Bosch, F. C., & Rest, A. 2001, *AJ*, 121, 2928
- van Dokkum, P. G., & Franx, M. 1995, *AJ*, 110, 1995

- van Driel, W., Arnaboldi, M., Combes, F., & Sparke, L. 2000, *A&AS*, 141, 385
- Verdoes Kleijn, G. A., Baum, S. A., de Zeeuw, P. T., & O’Dea, C. P. 1999, *AJ*, 118, 2592
- Wang, Z., Schweizer, F., & Scoville, N. Z. 1992, *ApJ*, 396, 510
- Wardle, M., & Knapp, G. R. 1986, *AJ*, 91, 23
- Welch, W. J. et al. 1996, *PASP*, 108, 93
- Wiklind, T., Combes, F., & Henkel, C. 1995, *A&A*, 297, 643 (WCH)
- Wiklind, T., Combes, F., Henkel, C., & Wyrowski, F. 1997, *A&A*, 323, 727
- Wiklind, T. & Henkel, C. 2001, *A&A*, 375, 797
- Wong, T. 2001, Ph.D. thesis, University of California at Berkeley.
- Young, L. M. 2000, *AJ*, 120, 2460

Table 5. Dynamical Masses

Galaxy	$i$ °	$V \sin i$ km s <sup>-1</sup>	$V$ km s <sup>-1</sup>	$R$ kpc	$M_{min}$ 10 <sup>10</sup> M <sub>⊙</sub>	$M_{max}$ 10 <sup>10</sup> M <sub>⊙</sub>	$M(\text{H}_2)/M_{dyn}$	$t_{orb}$ 10 <sup>8</sup> yr
UGC 1503	51	130 (10)	167 (13)	5.5 (0.6)	2.2	3.6	0.050–0.082	2.0
NGC 807	65	230 (10)	254 (11)	6.2 (0.6)	7.6	9.3	0.015–0.018	1.5
NGC 3656	74	270 (10)	280 (10)	3.7 (0.4)	6.3	6.8	0.070–0.075	0.82
NGC 4476	65	100 (10)	110 (11)	1.2 (0.1)	0.27	0.34	0.034–0.042	0.66
NGC 5666	27	100 (20)	217 (43)	2.4 (0.2)	0.55	2.6	0.022–0.10	0.75

Note. — The inclination angle  $i$  of the gas disk is given by  $\cos i = 1 - \epsilon$ , with  $\epsilon$  given in Table 4. If the gas disk is not thin,  $i$  is a lower limit, and the true circular velocity will be somewhere between  $V \sin i$  and  $V$ ; the enclosed dynamical mass will be between  $M_{min}$  and  $M_{max}$ . The range in  $M(\text{H}_2)/M_{dyn}$  comes from the range in the enclosed dynamical mass, ignoring the uncertainty in the  $\text{H}_2/\text{CO}$  conversion factor, which is probably at least 50% to 100%.

Table 6. Alignment with Optical Major Axis

Galaxy	Radii "	Optical Morphology		Misalignment
		$\epsilon$	PA ( $^\circ$ )	$ \Delta\text{PA} $ ( $^\circ$ )
UGC 1503	10–27	0.21 (0.02)	–124 (2)	1 (3)
NGC 807	10–30	0.35 (0.05)	140 (1)	9 (3)
NGC 3656	...	0.20 (0.04)	110 (5)	81 (6)
NGC 4476	10–30	0.35 (0.02)	–155 (1)	3 (2)
NGC 5666	10–20	0.14 (0.02)	151 (4)	13 (5)

Note. — Optical ellipticities and position angles are mean values over the semimajor axis range indicated under “Radii.” Optical morphology information for NGC 3656 is taken from Balcells (1997) so is not restricted by the overexposed/underexposed regions of the DSS. The parenthesized values in the  $\epsilon$  and PA columns are the dispersion about the mean  $\epsilon$  and PA over that radius range. Because these dispersions are normally larger than the formal fit uncertainties, they indicate something about the magnitude of possible radial variations in  $\epsilon$  and PA. The misalignment angle  $\Delta\text{PA}$  is the difference between the molecular gas’s kinematic PA (Table 4) and the optical major axis PA.